SAND2018-9255PE

Atom interferometer model

Daniel Soh

Sandia National Laboratories

August 21, 2018

Contents

1 Introduction

This is a technical note describing the Simulink block modeling the dynamics of the atom interferometer. The theory part is largely based on the PhD thesis by Rakholia [1].

2 Theory

2.1 Evolution under light

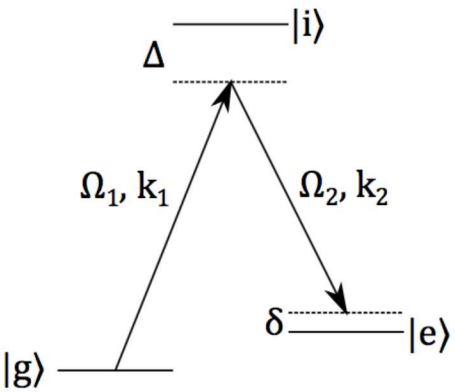

(a) Raman transition

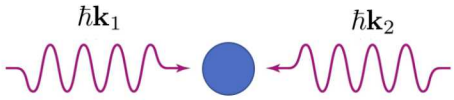

(b) Atom under two laser fields

Figure 2.1: Schematic of the Raman transition (left) used for the Doppler sensitive transition. Picture taken from Rakholia [1]. Also the atom under the influence of two laser fields is shown (right).

Let us consider an atom with three energy eigenstates under the influence of two laser fields as shown in Figure 2.1. The first laser field is resonant with $|g\rangle \to |i\rangle$ with an offset Δ, and the second is resonant with $|i\rangle \to |e\rangle$ with an additional offset δ. Let us assume that the atom has an initial momentum $\boldsymbol{p}_0$, and in the ground state. Then initial state is then $|g\rangle \otimes |\boldsymbol{p}_0\rangle$. If the atom absorbs the photon with a momentum $\hbar\boldsymbol{k}_1$, the atom gains the same amount of momentum and the state is $|i\rangle \otimes |\boldsymbol{p}_0 + \hbar\boldsymbol{k}_1\rangle$. Without emitting any photon through spontaneous emission (since Δ is very large), the atom may undergo the stimulated emission by the photon having a momentum $\hbar\boldsymbol{k}_2$. The final state after the two photon absorption process is $|e\rangle \otimes |\boldsymbol{p}_0 + \hbar\boldsymbol{k}_{\text{eff}}\rangle$ where $\boldsymbol{k}_{\text{eff}} = \boldsymbol{k}_1 - \boldsymbol{k}_2$ ($|\boldsymbol{k}_{\text{eff}}| = |\boldsymbol{k}_1| + |\boldsymbol{k}_2|$ since $\boldsymbol{k}_1$ is opposite to $\boldsymbol{k}_2$).

Let us first study the quantum state evolution for an atom at a fixed position $\boldsymbol{x}$. The Hilbert space is three dimensional with the orthonormal basis of $\{|g\rangle, |e\rangle, |i\rangle\}$. The unperturbed Hamiltonian is given as

$$H_0 = \hbar\omega_{eg} |e\rangle\langle e| + \hbar\omega_{ig} |i\rangle\langle i|, \tag{2.1}$$

where $\hbar\omega_{eg}$ is the energy between $|e\rangle$ and $|g\rangle$ and $\hbar\omega_{ig}$ is that between $|i\rangle$ and $|g\rangle$. The interaction Hamiltonian is given as

$$H_I = -\boldsymbol{d} \cdot \boldsymbol{E}, \tag{2.2}$$

where $\boldsymbol{d}$ is the dipole moment of the atom, and the electric field is given by

$$\boldsymbol{E} = \frac{1}{2}\boldsymbol{E}_1 \mathrm{e}^{i(\boldsymbol{k}_1\cdot\boldsymbol{x}-\omega_1 t)} + \frac{1}{2}\boldsymbol{E}_2 \mathrm{e}^{i(\boldsymbol{k}_2\cdot\boldsymbol{x}-\omega_2 t)} + \text{c.c.}, \tag{2.3}$$

where $|\boldsymbol{k}_i| = 2\pi/\lambda_i$ with $i = 1, 2$ and λ_i are the wavelengths of the incoming light fields. Let us define the Rabi oscillation frequencies as

$$\begin{aligned}\Omega_1 &= -\frac{1}{2\hbar}\langle g|\, \boldsymbol{d}\cdot\boldsymbol{E}_1\, |i\rangle\,,\\ \Omega_2 &= -\frac{1}{2\hbar}\langle e|\, \boldsymbol{d}\cdot\boldsymbol{E}_2\, |i\rangle\,.\end{aligned} \tag{2.4}$$

Then, the interaction Hamiltonian is

$$H_I = \hbar\Omega_1^* \mathrm{e}^{i(\boldsymbol{k}_1\cdot\boldsymbol{x}_g-\omega_1 t)}\, |i\rangle\langle g| + \hbar\Omega_2^* \mathrm{e}^{i(\boldsymbol{k}_2\cdot\boldsymbol{x}_e-\omega_2 t)}\, |i\rangle\langle e| + \text{h.c.}, \tag{2.5}$$

where h.c. stands for Hermite conjugate. Here, we assume the dipole approximation where the atomic wave function is much smaller than the light wavelength, and the light has a fixed phase over the atomic spatial wave function. Note also that the phase of the interaction matters, particularly the dependence on the positions: $\boldsymbol{x}_{g,e}$ represents the position of the particle in $|g, e\rangle$ states, respectively.

The Schrödinger equation is

$$i\hbar\partial_t\, |\psi(t)\rangle = (H_0 + H_I)\, |\psi(t)\rangle\,, \tag{2.6}$$

where we ignore the loss channels, and the state is in general given by

$$|\psi(t)\rangle = c_g(t)\, |g\rangle + c_i(t)\, |i\rangle + c_e(t)\, |e\rangle\,, \tag{2.7}$$

with the normalization $|c_g(t)|^2 + |c_i(t)|^2 + |c_e(t)|^2 = 1$. Then, it easily follows that

$$\begin{aligned} i\hbar\dot{c_g} &= \hbar\Omega_1 \mathrm{e}^{i(-\boldsymbol{k}_1\cdot\boldsymbol{x}_g+\omega_1 t)} c_i,\\ i\hbar\dot{c_e} &= \hbar\Omega_2 \mathrm{e}^{i(-\boldsymbol{k}_2\cdot\boldsymbol{x}_e+\omega_2 t)} c_i + \hbar\omega_{eg} c_e,\\ i\hbar\dot{c_i} &= \hbar\Omega_1^* \mathrm{e}^{i(\boldsymbol{k}_1\cdot\boldsymbol{x}_g-\omega_1 t)} c_g + \hbar\Omega_2^* \mathrm{e}^{i(\boldsymbol{k}_2\cdot\boldsymbol{x}_e-\omega_2 t)} c_e + \hbar\omega_{ig} c_i. \end{aligned} \tag{2.8}$$

Replacing

$$\begin{aligned} c_g &= \tilde{c}_g,\\ c_e &= \tilde{c}_e \mathrm{e}^{-i\omega_{eg} t},\\ c_i &= \tilde{c}_i \mathrm{e}^{-i\omega_{ig} t}, \end{aligned} \tag{2.9}$$

we obtain

$$\begin{aligned} i\dot{\tilde{c}}_g &= \Omega_1 \mathrm{e}^{-i(\boldsymbol{k}_1\cdot\boldsymbol{x}_g+\Delta t)} \tilde{c}_i,\\ i\dot{\tilde{c}}_e &= \Omega_2 \mathrm{e}^{-i(\boldsymbol{k}_2\cdot\boldsymbol{x}_e+(\Delta+\delta) t)} \tilde{c}_i,\\ i\dot{\tilde{c}}_i &= \Omega_1^* \mathrm{e}^{i(\boldsymbol{k}_1\cdot\boldsymbol{x}_g+\Delta t)} \tilde{c}_g + \Omega_2^* \mathrm{e}^{i(\boldsymbol{k}_2\cdot\boldsymbol{x}_e+(\Delta+\delta) t)} \tilde{c}_e, \end{aligned} \tag{2.10}$$

where we define the detuning parameters as

$$\begin{aligned}\Delta &= \omega_{ig} - \omega_1, \\ \delta &= \omega_1 - \omega_2 - \omega_{eg}.\end{aligned} \tag{2.11}$$

Assuming $\Delta \gg \Omega_1, \Omega_2, \delta$, we can apply the adiabatic elimination procedure where, to solve $\tilde{c}_i$ dynamics, we assume $\tilde{c}_g, \tilde{c}_e$ to be constant since the dynamics of $\tilde{c}_i$ is very fast. Integrating $\dot{\tilde{c}}_i$ from the third equation in equation (2.10), we obtain

$$\tilde{c}_i = -\frac{\Omega_1^*}{\Delta} \mathrm{e}^{i(\boldsymbol{k}_1 \cdot \boldsymbol{x}_g + \Delta t)} \tilde{c}_g - \frac{\Omega_2^*}{\Delta} \mathrm{e}^{i(\boldsymbol{k}_2 \cdot \boldsymbol{x}_e + (\Delta+\delta)t)} \tilde{c}_e, \tag{2.12}$$

where in the second term, we approximated $\Omega_2^*/(\Delta + \delta) \approx \Omega_2^*/\Delta$. Using this, we finally obtain the quasi-two-level dynamical equation:

$$\begin{aligned}\dot{\tilde{c}}_g &= i\frac{|\Omega_1|^2}{\Delta}\tilde{c}_g + i\frac{\Omega_1\Omega_2^*}{\Delta}\tilde{c}_e \mathrm{e}^{i(\boldsymbol{k}_2 \cdot \boldsymbol{x}_e - \boldsymbol{k}_1 \cdot \boldsymbol{x}_g + \delta t)}, \\ \dot{\tilde{c}}_e &= i\frac{\Omega_1^*\Omega_2}{\Delta} \mathrm{e}^{i(\boldsymbol{k}_1 \cdot \boldsymbol{x}_g - \boldsymbol{k}_2 \cdot \boldsymbol{x}_e - \delta t)} \tilde{c}_g + i\frac{|\Omega_2|^2}{\Delta}\tilde{c}_e.\end{aligned} \tag{2.13}$$

The above is easy to solve by replacing

$$\tilde{c}_g(t) = x(t)\mathrm{e}^{i\frac{|\Omega_1|^2}{\Delta}t}, \quad \tilde{c}_e(t) = y(t)\mathrm{e}^{i\frac{|\Omega_2|^2}{\Delta}t}, \tag{2.14}$$

which transforms the differential equations to the following with $\Delta_{kx} = \boldsymbol{k}_1 \cdot \boldsymbol{x}_g - \boldsymbol{k}_2 \cdot \boldsymbol{x}_e$:

$$\begin{aligned}\dot{x} &= i\frac{\Omega_1\Omega_2^*}{\Delta} y \mathrm{e}^{iDt - i\Delta_{kx}}, \\ \dot{y} &= i\frac{\Omega_1^*\Omega_2}{\Delta} x \mathrm{e}^{-iDt + i\Delta_{kx}},\end{aligned} \tag{2.15}$$

where

$$D = \frac{|\Omega_2|^2 - |\Omega_1|^2}{\Delta} + \delta. \tag{2.16}$$

The solution is easily obtained as

$$\begin{aligned}x(t) &= \mathrm{e}^{+i\frac{D}{2}t}\left[x_0\left(\cos\left(\frac{D'}{2}t\right) + \frac{D}{D'}i\sin\left(\frac{D'}{2}t\right)\right) - i2y_0\mathrm{e}^{-i\Delta_{kx}}\frac{\Omega_1\Omega_2^*}{\Delta D'}\sin\left(\frac{D'}{2}t\right)\right], \\ y(t) &= \mathrm{e}^{-i\frac{D}{2}t}\left[y_0\left(\cos\left(\frac{D'}{2}t\right) - \frac{D}{D'}i\sin\left(\frac{D'}{2}t\right)\right) - i2x_0\mathrm{e}^{i\Delta_{kx}}\frac{\Omega_1^*\Omega_2}{\Delta D'}\sin\left(\frac{D'}{2}t\right)\right],\end{aligned} \tag{2.17}$$

where

$$D' = \sqrt{D^2 + 4\frac{|\Omega_1|^2|\Omega_2|^2}{\Delta^2}} = \sqrt{\frac{(|\Omega_1|^2 + |\Omega_2|^2)^2}{\Delta^2} + \delta^2 + 2\frac{\delta}{\Delta}(|\Omega_2|^2 - |\Omega_1|^2)} \tag{2.18}$$

Therefore, we finally obtain

$$c_g(t) = \mathrm{e}^{+i\left(\frac{|\Omega_1|^2+|\Omega_2|^2}{2\Delta}+\frac{\delta}{2}\right)t}\left[c_g(0)\left(\cos\left(\frac{D'}{2}t\right)+\frac{D}{D'}i\sin\left(\frac{D'}{2}t\right)\right)-2ic_e(0)\mathrm{e}^{-i\Delta_{kx}}\frac{\Omega_1\Omega_2^*}{\Delta D'}\sin\left(\frac{D'}{2}t\right)\right],$$
$$c_e(t) = \mathrm{e}^{-i\left(\omega_{eg}-\frac{|\Omega_1|^2+|\Omega_2|^2}{2\Delta}+\frac{\delta}{2}\right)t}\left[c_e(0)\left(\cos\left(\frac{D'}{2}t\right)-\frac{D}{D'}i\sin\left(\frac{D'}{2}t\right)\right)-2ic_g(0)\mathrm{e}^{i\Delta_{kx}}\frac{\Omega_1^*\Omega_2}{\Delta D'}\sin\left(\frac{D'}{2}t\right)\right], \tag{2.19}$$

Let us examine particularly the case where $c_g(0) = 1$ and $c_e(0) = 0$ (the ground state of the atom). In this case we have

$$c_g(t) = \mathrm{e}^{+i\left(\frac{|\Omega_1|^2+|\Omega_2|^2}{2\Delta}+\frac{\delta}{2}\right)t}\left(\cos\left(\frac{D'}{2}t\right)+\frac{D}{D'}i\sin\left(\frac{D'}{2}t\right)\right),$$
$$c_e(t) = -i\mathrm{e}^{-i\left(\omega_{eg}-\frac{|\Omega_1|^2+|\Omega_2|^2}{2\Delta}+\frac{\delta}{2}\right)t}\mathrm{e}^{i\Delta_{kx}}\frac{2\Omega_1^*\Omega_2}{\Delta D'}\sin\left(\frac{D'}{2}t\right). \tag{2.20}$$

Suppose that $|D'| \gg |D|$ (i.e., $|\Omega_1\Omega_2|/\Delta \gg |(|\Omega_2|^2 - |\Omega_1|^2)/\Delta + \delta|$). This approximately implies that

$$|c_g(t)|^2 \approx \cos^2(D't/2), \quad |c_e(t)|^2 \approx \sin^2(D't/2). \tag{2.21}$$

Therefore, at time $t = \pi/D'$, the state is inverted. On the other hand, at time $t = \pi/2D'$, one can make a linear superposition between $|g\rangle$ and $|e\rangle$. Hence, one can adjust the light pulse duration to bring the state to either linear superposition state or the inverted state. Note that $\Delta_{kx} = \boldsymbol{k}_1 \cdot \boldsymbol{x}_g - \boldsymbol{k}_2 \cdot \boldsymbol{x}_e$ is inscribed only on c_e in this case.

Let us call the optical pulse with duration $t = \pi/D'$ as 'π' pulse and that with duration $t = \pi/2D'$ as '$\pi/2$' pulse. Then, we understand that the π pulse inverts the state between $|e\rangle$ and $|g\rangle$, while $\pi/2$ pulse makes a superposition state.

In more details, we can express the equation (2.17) in a matrix form,

$$\begin{pmatrix} x(t) \\ y(t) \end{pmatrix} = U(t)\begin{pmatrix} x(0) \\ y(0) \end{pmatrix},$$
$$U(t) = \begin{pmatrix} \mathrm{e}^{+i\frac{D}{2}t}\left(\cos\left(\frac{D'}{2}t\right)+\frac{D}{D'}i\sin\left(\frac{D'}{2}t\right)\right) & -i\mathrm{e}^{+i\frac{D}{2}t-i\Delta_{kx}}\frac{\Omega_{\mathrm{eff}}}{D'}\sin\left(\frac{D'}{2}t\right) \\ -i\mathrm{e}^{+i\Delta_{kx}-i\frac{D}{2}t}\frac{\Omega_{\mathrm{eff}}^*}{D'}\sin\left(\frac{D'}{2}t\right) & \mathrm{e}^{-i\frac{D}{2}t}\left(\cos\left(\frac{D'}{2}t\right)-\frac{D}{D'}i\sin\left(\frac{D'}{2}t\right)\right) \end{pmatrix}, \tag{2.22}$$

where $\Omega_{\mathrm{eff}} = 2\Omega_1\Omega_2^*/\Delta$. Then, it is easily verified that $U^\dagger(t)U(t) = \mathbf{1}$, an identity matrix so that $U(t)$ is a unitary transformation matrix preserving $|x(t)|^2 + |y(t)|^2 = |\tilde{c}_g(t)|^2 + |\tilde{c}_e(t)|^2 = 1$ for all the time t.

For $t = \pi/D'$ and $t = \pi/2D'$, we obtain

$$U\left(\frac{\pi}{D'}\right) = \begin{pmatrix} \mathrm{e}^{i\frac{D\pi}{2D'}}\frac{D}{D'}i & -i\mathrm{e}^{i\frac{D\pi}{2D'}-i\Delta_{kx}}\frac{\Omega_{\mathrm{eff}}}{D'} \\ -i\mathrm{e}^{-i\frac{D\pi}{2D'}+i\Delta_{kx}}\frac{\Omega_{\mathrm{eff}}^*}{D'} & \mathrm{e}^{-i\frac{D\pi}{2D'}}\frac{D}{D'}i \end{pmatrix},$$
$$U\left(\frac{\pi}{2D'}\right) = \frac{1}{\sqrt{2}}\begin{pmatrix} \mathrm{e}^{i\frac{D\pi}{4D'}}\left(1+\frac{D}{D'}i\right) & -i\mathrm{e}^{i\frac{D\pi}{4D'}-i\Delta_{kx}}\frac{\Omega_{\mathrm{eff}}}{D'} \\ -i\mathrm{e}^{-i\frac{D\pi}{4D'}+i\Delta_{kx}}\frac{\Omega_{\mathrm{eff}}}{D'} & \mathrm{e}^{-i\frac{D\pi}{4D'}}\left(1-\frac{D}{D'}i\right) \end{pmatrix}. \tag{2.23}$$

Note that for the case $|D| \ll |D'|$, we have $|\Omega_{\mathrm{eff}}| \approx |D'|$, and hence, for the case where

Ω_{eff} is real and positive, we obtain

$$U\left(\frac{\pi}{D'}\right) \approx \begin{pmatrix} 0 & -ie^{-i\Delta_{kx}} \\ -ie^{+i\Delta_{kx}} & 0 \end{pmatrix}, \quad U\left(\frac{\pi}{2D'}\right) \approx \frac{1}{\sqrt{2}} \begin{pmatrix} 1 & -ie^{-i\Delta_{kx}} \\ -ie^{+i\Delta_{kx}} & 1 \end{pmatrix}. \tag{2.24}$$

The pulses Ω_1 and Ω_2 that causes the transfer matrix $U(\pi/D')$ is called π pulse, and the effect of π pulse is reversing the population. The pulses Ω_1 and Ω_2 that causes the transfer matrix $U(\pi/2D')$ is called $\pi/2$ pulse, and the effect of $\pi/2$ pulse is the 50:50 beam splitter that splits the population equally.

2.2 Accelerometer

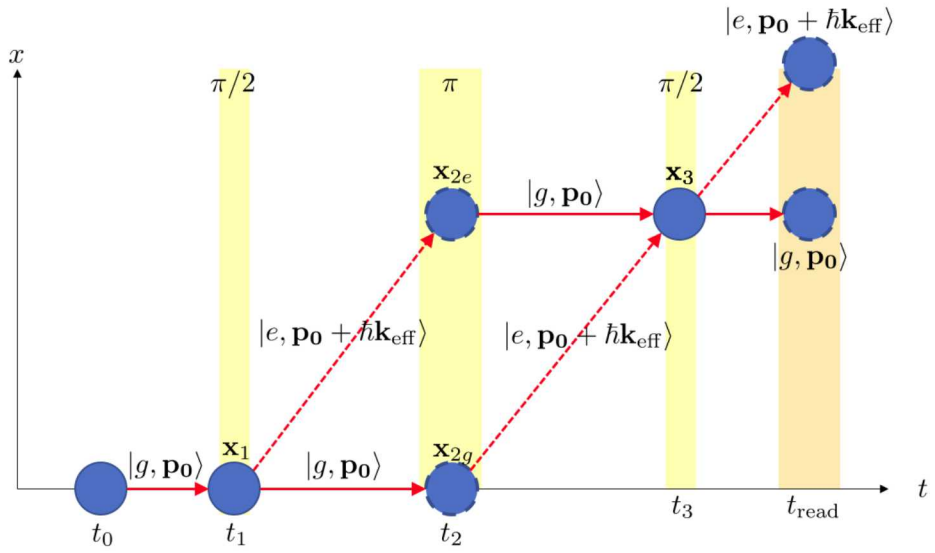

Figure 2.2: Schematic of an atom interferometer accelerometer.

The atom interferometer can be used as an accelerometer as shown in figure 2.2. At time t_0, the atom is cooled in a magneto-optic trap (MOT), having the initial momentum $\boldsymbol{p}_0$. The state at t_0 is

$$|\psi(t_0)\rangle = |g, \boldsymbol{p}_0\rangle\,. \tag{2.25}$$

A $\pi/2$ light pulse at time t_1 turns the state of a superposition of the $|g, \boldsymbol{p}_0\rangle$ and $|e, \boldsymbol{p}_0 + \hbar\boldsymbol{k}_{\text{eff}}\rangle$. The $\pi/2$ pulse operates a atomic wave function splitter, having a transfer matrix in the basis $\{|g, \boldsymbol{p}_0\rangle, |e, \boldsymbol{p}_0 + \hbar\boldsymbol{k}_{\text{eff}}\rangle\}$ (equation (2.24)):

$$R_1 = \frac{1}{\sqrt{2}} \begin{pmatrix} 1 & -ie^{-i\boldsymbol{k}_{\text{eff}}\cdot\boldsymbol{x}_1} \\ -ie^{+i\boldsymbol{k}_{\text{eff}}\cdot\boldsymbol{x}_1} & 1 \end{pmatrix}, \tag{2.26}$$

where $\boldsymbol{k}_{\text{eff}} = \boldsymbol{k}_1 - \boldsymbol{k}_2$ and $\boldsymbol{x}_1$ is the atom position at time t_1. Recall that the light phase signature $+\boldsymbol{k}_{\text{eff}} \cdot \boldsymbol{x}_1$ is added only to the transition $|g\rangle \to |e\rangle$ while $-\boldsymbol{k}_{\text{eff}} \cdot \boldsymbol{x}_1$ is added to the transition $|e\rangle \to |g\rangle$ (see equation (2.19)).

A π light pulse at time t_2 turns the state inverted (acting as a 'mirror'), turning $|g\rangle \to |e\rangle$ and $|e\rangle \to |g\rangle$, with the light signature phase of the position $\boldsymbol{x}_{2e}$ for the part in $|e, \boldsymbol{p}_0 + \hbar\boldsymbol{k}_{\text{eff}}\rangle$ and $\boldsymbol{x}_{2g}$ for the part in $|g, \boldsymbol{p}_0\rangle$. Note that each state has a different position, warranting to solve the differential equation of the state at a fixed position to be solved

separately, and later be superposed. Then, the transfer matrix is (see equation (2.24))

$$R_2 = \begin{pmatrix} 0 & -i\mathrm{e}^{-i(\boldsymbol{k}_1\cdot\boldsymbol{x}_{2g}-\boldsymbol{k}_2\cdot\boldsymbol{x}_{2e})} \\ -i\mathrm{e}^{+i(\boldsymbol{k}_1\cdot\boldsymbol{x}_{2g}-\boldsymbol{k}_2\cdot\boldsymbol{x}_{2e})} & 0 \end{pmatrix}. \tag{2.27}$$

A $\pi/2$ light pulse at time t_3 turns the state using the similar transfer matrix with the position $\boldsymbol{x}_3$ (see equation (2.24))

$$R_3 = \frac{1}{\sqrt{2}}\begin{pmatrix} 1 & -i\mathrm{e}^{-i\boldsymbol{k}_{\mathrm{eff}}\cdot\boldsymbol{x}_3} \\ -i\mathrm{e}^{+i\boldsymbol{k}_{\mathrm{eff}}\cdot\boldsymbol{x}_3} & 1 \end{pmatrix}, \tag{2.28}$$

The pulse timing is such that $t_2 - t_1 = T = t_3 - t_2$. Then, the time dependence of the phase is eliminated, and only the position dependent light signature is left. Then, the final state is calculated as

$$|\psi(t_{\mathrm{read}})\rangle = R_3 R_2 R_1 |\psi(t_0)\rangle, \tag{2.29}$$

where $|\psi(t_0)\rangle = |g, \boldsymbol{p}_0\rangle = \begin{pmatrix} 1 \\ 0 \end{pmatrix}$. The result is that

$$|\psi(t_{\mathrm{eff}})\rangle = c_g(t_{\mathrm{read}})\,|g, \boldsymbol{p}_0\rangle + c_e(t_{\mathrm{read}})\,|e, \boldsymbol{p}_0 + \hbar\boldsymbol{k}_{\mathrm{eff}}\rangle, \tag{2.30}$$

where

$$\begin{aligned} c_g(t_{\mathrm{read}}) &= -\frac{1}{2}\mathrm{e}^{-i(\boldsymbol{k}_2\cdot(\boldsymbol{x}_1+\boldsymbol{x}_{2e})+\boldsymbol{k}_1\cdot(\boldsymbol{x}_{2g}+\boldsymbol{x}_3))}\left(\mathrm{e}^{i(2\boldsymbol{k}_2\cdot\boldsymbol{x}_{2e}+\boldsymbol{k}_1\cdot(\boldsymbol{x}_1+\boldsymbol{x}_3))} + \mathrm{e}^{i(2\boldsymbol{k}_1\cdot\boldsymbol{x}_{2g}+\boldsymbol{k}_2\cdot(\boldsymbol{x}_1+\boldsymbol{x}_3))}\right) \\ c_e(t_{\mathrm{read}}) &= i\frac{1}{2}\mathrm{e}^{-i(\boldsymbol{k}_2\cdot(\boldsymbol{x}_1+\boldsymbol{x}_{2e}+\boldsymbol{x}_3)+\boldsymbol{k}_1\cdot\boldsymbol{x}_{2g})}\left(-\mathrm{e}^{i(2\boldsymbol{k}_2\cdot\boldsymbol{x}_{2e}+\boldsymbol{k}_1\cdot(\boldsymbol{x}_1+\boldsymbol{x}_3))} + \mathrm{e}^{i(2\boldsymbol{k}_1\cdot\boldsymbol{x}_{2g}+\boldsymbol{k}_2\cdot(\boldsymbol{x}_1+\boldsymbol{x}_3))}\right). \end{aligned} \tag{2.31}$$

Hence, the population ratio is

$$\frac{|c_e(t_{\mathrm{read}})|^2}{|c_g(t_{\mathrm{read}})|^2} = \tan^2\left[\frac{1}{2}\left(2\boldsymbol{k}_2\cdot\boldsymbol{x}_{2e} + \boldsymbol{k}_{\mathrm{eff}}\cdot(\boldsymbol{x}_1+\boldsymbol{x}_3) - 2\boldsymbol{k}_1\cdot\boldsymbol{x}_{2g}\right)\right]. \tag{2.32}$$

We now approximate $\boldsymbol{k}_2 \approx -\boldsymbol{k}_1$, implying that $\boldsymbol{k}_1 \approx \boldsymbol{k}_{\mathrm{eff}}/2$, $\boldsymbol{k}_2 \approx -\boldsymbol{k}_{\mathrm{eff}}/2$. With this approximation, one obtains

$$\frac{|c_e(t_{\mathrm{read}})|^2}{|c_g(t_{\mathrm{read}})|^2} = \tan^2\left[\frac{1}{2}\boldsymbol{k}_{\mathrm{eff}}\cdot(\boldsymbol{x}_1 - \boldsymbol{x}_{2e} - \boldsymbol{x}_{2g} + \boldsymbol{x}_3)\right]. \tag{2.33}$$

We note the quantity:

$$\boldsymbol{x}_1 - \boldsymbol{x}_{2e} - \boldsymbol{x}_{2g} + \boldsymbol{x}_3 \approx T^2\ddot{\boldsymbol{x}} = T^2\left(\boldsymbol{a} - 2\boldsymbol{v}\times\boldsymbol{\Omega}\right), \tag{2.34}$$

where $\boldsymbol{a}$ is the acceleration applied to the apparatus, $\boldsymbol{v} = \boldsymbol{p}_0/M$ is the initial velocity of the atom with the atom mass M, and $\boldsymbol{\Omega}$ is the rotation rate that the apparatus undergoes. Therefore, measuring the population ratio between the two states in equation (2.32) reveals the acceleration and the rotation rate. Combining the above two equations, we obtain

$$|\boldsymbol{a} - 2\boldsymbol{v}\times\boldsymbol{\Omega}| = \frac{2}{T^2|\boldsymbol{k}_{\mathrm{eff}}|\cos\theta}\mathrm{atan}\left(\frac{|c_e(t_{\mathrm{read}})|}{|c_g(t_{\mathrm{read}})|}\right), \tag{2.35}$$

where θ is the angle between $\boldsymbol{k}_{\text{eff}}$ and $\boldsymbol{a} - 2\boldsymbol{v} \times \boldsymbol{\Omega}$.

3 Matlab Simulink block model

For simulating the atom interferometer accelerometer, we need a dynamical equation to describe the behavior of the degrees of freedom. We could start from the equation (2.8) that contains the population in $|i\rangle$ level. However, for simplicity for the first cut model, we adopt the adiabatic elimination step assuming $\Delta \gg \Omega_1, \Omega_2, \delta$, and leave the dynamics of $|e\rangle, |i\rangle$ only.

3.1 Simulink dynamics sequence

We use the equation (2.13) to describe the internal dynamics of the atom interferometer. We restore the approximation back to have

$$\begin{aligned}
\dot{\tilde{c}}_g &= i\frac{|\Omega_1|^2}{\Delta}\tilde{c}_g + i\frac{\Omega_1\Omega_2^*}{\Delta+\delta}\tilde{c}_e \mathrm{e}^{i(\boldsymbol{k}_2\cdot\boldsymbol{x}_e - \boldsymbol{k}_1\cdot\boldsymbol{x}_g + \delta t)}, \\
\dot{\tilde{c}}_e &= i\frac{\Omega_1^*\Omega_2}{\Delta}\mathrm{e}^{i(\boldsymbol{k}_1\cdot\boldsymbol{x}_g - \boldsymbol{k}_2\cdot\boldsymbol{x}_e - \delta t)}\tilde{c}_g + i\frac{|\Omega_2|^2}{\Delta+\delta}\tilde{c}_e.
\end{aligned} \tag{3.1}$$

To be clear, we write down the description of the following parameters connecting to the physical quantities:

$$\begin{aligned}
\boldsymbol{E}(\boldsymbol{x},t) &= \frac{1}{2}\boldsymbol{E}_1(t)\mathrm{e}^{i(\boldsymbol{k}_1\cdot\boldsymbol{x}-\omega_1 t)} + \frac{1}{2}\boldsymbol{E}_2(t)\mathrm{e}^{i(\boldsymbol{k}_2\cdot\boldsymbol{x}-\omega_2 t)} + \text{c.c.}, \\
\Omega_1(t) &= -\frac{1}{2\hbar}\langle g|\,\boldsymbol{d}\cdot\boldsymbol{E}_1(t)\,|i\rangle\,, \\
\Omega_2(t) &= -\frac{1}{2\hbar}\langle e|\,\boldsymbol{d}\cdot\boldsymbol{E}_2(t)\,|i\rangle\,, \\
\boldsymbol{k}_{\text{eff}} &= \boldsymbol{k}_1 - \boldsymbol{k}_2,
\end{aligned} \tag{3.2}$$

with the usual photon propagation constants $|\boldsymbol{k}_i| = 2\pi/\lambda_i$ where λ_i is the wavelength of the light. Here, $\boldsymbol{E}_i(t)$ is a time-dependent, slowly-varying, complex amplitude of the driving light. Note that if no light is applied (i.e., $\Omega_{1,2} = 0$), $\dot{\tilde{c}}_{g,e} = 0$, and hence, no change occurs.

We follow the sequence shown in figure 2.2. The matlab simulink block performs the quantum simulation as follows:

- At time t_1, the atom is purely at $|g\rangle$ state, and the position of atom is well defined at $\boldsymbol{x}_1$. The input light turns on Ω_1 and Ω_2, starts running the dynamics shown in equation (3.1). At the end of this fist pulse, the atom wave function is split into two $c_g(t_1)$ and $c_e(t_1)$.

- Until time t_2, the two wave functions c_g and c_e separates the atom position according to their momentum $\boldsymbol{p}_0$ and $\boldsymbol{p}_0 + \hbar\boldsymbol{k}_{\text{eff}}$, respectively. As a result, the two wave

functions have different atom position at

$$\begin{aligned}\boldsymbol{x}_{2g} &= \boldsymbol{a}_{\text{tot}}\frac{T^2}{2} + \frac{\boldsymbol{p}_0}{M}T + \boldsymbol{x}_1,\\ \boldsymbol{x}_{2e} &= \boldsymbol{a}_{\text{tot}}\frac{T^2}{2} + \left(\frac{\boldsymbol{p}_0 + \hbar\boldsymbol{k}_{\text{eff}}}{M}\right)T + \boldsymbol{x}_1,\end{aligned} \tag{3.3}$$

where $T = t_2 - t_1$, $\boldsymbol{a}_{\text{tot}} = \boldsymbol{a} - 2\boldsymbol{v}\times\boldsymbol{\Omega}$ and M is mass of the atom.

- At time t_2, we perform the quantum evolution in equation (3.2), but at two different locations. In both locations, the initial conditions are the same that is the output of the t_1 beam splitter. The final wave functions will be produced for both c_g and c_e.

- We then have two different states: from $\boldsymbol{x}_{2g}$,

$$|\psi_g(t_2)\rangle = c_{gg}(t_2)\,|g, \boldsymbol{p}_0, \boldsymbol{x}_{2g}\rangle + c_{eg}(t_2)\,|e, \hbar\boldsymbol{p}_0 + \hbar\boldsymbol{k}_{\text{eff}}, \boldsymbol{x}_{2g}\rangle\,, \tag{3.4}$$

  while from $\boldsymbol{x}_{2e}$,

$$|\psi_e(t_2)\rangle = c_{ge}(t_2)\,|g, \boldsymbol{p}_0, \boldsymbol{x}_{2e}\rangle + c_{ee}(t_2)\,|e, \hbar\boldsymbol{p}_0 + \hbar\boldsymbol{k}_{\text{eff}}, \boldsymbol{x}_{2e}\rangle\,. \tag{3.5}$$

  In addition, the total wave function is

$$|\psi(t_2)\rangle = c_g(t_1)\,|\psi_g(t_2)\rangle + c_e(t_1)\,|\psi_e(t_2)\rangle\,. \tag{3.6}$$

- Until time t_3, the four different individual states $\left|g, \boldsymbol{p}_0, \boldsymbol{x}_{2g/2e}\right\rangle$ and $\left|e, \boldsymbol{p}_0 + \hbar\boldsymbol{k}_{\text{eff}}, \boldsymbol{x}_{2g/2e}\right\rangle$ propagates according to the individual momenta (velocities) and the positions. Then, the four individual states arrive at time t_3 as follows. For simplicity, we assume that $t_3 - t_2 = T = t_2 - t_1$:

$$\begin{aligned}\boldsymbol{x}_{3gg} &= 2\boldsymbol{a}_{\text{tot}}T^2 + \frac{\boldsymbol{p}_0}{M}2T + \boldsymbol{x}_1,\\ \boldsymbol{x}_{3eg} &= 2\boldsymbol{a}_{\text{tot}}T^2 + \frac{2\boldsymbol{p}_0 + \hbar\boldsymbol{k}_{\text{eff}}}{M}T + \boldsymbol{x}_1,\\ \boldsymbol{x}_{3ge} &= 2\boldsymbol{a}_{\text{tot}}T^2 + \frac{2\boldsymbol{p}_0 + \hbar\boldsymbol{k}_{\text{eff}}}{M}T + \boldsymbol{x}_1,\\ \boldsymbol{x}_{3ee} &= 2\boldsymbol{a}_{\text{tot}}T^2 + \frac{2\boldsymbol{p}_0 + 2\hbar\boldsymbol{k}_{\text{eff}}}{M}T + \boldsymbol{x}_1,\end{aligned} \tag{3.7}$$

  Note that $\boldsymbol{x}_{3eg} = \boldsymbol{x}_{3ge}$.

- At time t_3, we perform the quantum evolution in equation (3.1), but at three different locations, at $\boldsymbol{x}_{3gg}$, $\boldsymbol{x}_{3ge} = \boldsymbol{x}_{3eg}$, and $\boldsymbol{x}_{3ee}$.

- For simplicity, we ignore the atom wave function at positions $\boldsymbol{x}_{3gg}$ and $\boldsymbol{x}_{3ee}$ in a good faith that the mirror π pulse at time t_2 would have completely inverted the states. This leaves the final state in

$$|\psi(t_3)\rangle = c_g(t_3)\,|g\rangle + c_e(t_3)\,|e\rangle\,. \tag{3.8}$$

- Finally, we perform the mapping in equation (2.35) using math functions.

The atom cloud has an initial momentum distribution for $\boldsymbol{p}_0$, following the Boltzmann distribution at a certain temperature. Therefore, in principle, one has to perform the above sequence for individual atoms having all different initial momentum $\boldsymbol{p}_0$. This complicates the calculation, and we will deal with this in detail in later models. But, for the initial model deployment, we simply assume a uniform atomic cloud having the same $\boldsymbol{p}_0$ and the same position $\boldsymbol{x}_1$.

3.2 Noise add on

The apparatus undergoes the acceleration given by $\boldsymbol{a}_{\text{tot}} = \boldsymbol{a} - 2\boldsymbol{v} \times \boldsymbol{\Omega}$. On top of this global acceleration, the MOT chamber may undergo additional accelerations, caused by the frame vibration. This extra noise acceleration must be added such that

$$\boldsymbol{a}_{\text{tot}} = \boldsymbol{a} - 2\boldsymbol{v} \times \boldsymbol{\Omega} + \boldsymbol{a}_N - 2\boldsymbol{v} \times \boldsymbol{\Omega_N}, \tag{3.9}$$

where $\boldsymbol{a}_N, \boldsymbol{\Omega_N}$ represent the added linear noise and the rotational noise. They could be well defined characteristic noises (having narrow frequency spectrum), or broadband ones, depending on the mechanical setup details. We will add this additional noise to the platform.

3.3 Description of block diagram

In order to simulate the atom interferometer accelerometer, we need to perform the coherent evolution of the population in $|g\rangle, |e\rangle$ states (see the differential equation in (3.1)). Additionally, we need to keep track of the movement of the individual atom wave functions to resolve the position correctly. Note that equations (3.3) and (3.7) are for the case where the acceleration $\boldsymbol{a}_{\text{tot}}$ is rather a constant over the entire measurement cycle. If the acceleration is time varying (particularly when the noise is strong), the equation is, for example,

$$\boldsymbol{x}_{2e}(t) = \int_0^t \mathrm{d}t' \left[\left(\int_0^{t'} \mathrm{d}t'' \boldsymbol{a}_{\text{tot}}(t'') \right) + \frac{\boldsymbol{p}_0 + \hbar \boldsymbol{k}_{\text{eff}}}{M} \right] + \boldsymbol{x}_1, \tag{3.10}$$

where, for clarity, $\boldsymbol{a}_{\text{tot}}(t) = \boldsymbol{a}(t) + \boldsymbol{a}_N(t)$ with the noise $\boldsymbol{a}_N(t)$. Since the total acceleration is time dependent, it is necessary to perform the simulation of the above dynamics.

Figure 3.1 shows the block diagram of the simulink block to simulate the atom interferometer accelerometer. The upper region is the kinetic dynamics part that solves the integral equations for the positions $\boldsymbol{x}_{2e}(t), \boldsymbol{x}_{2g}(t), \boldsymbol{x}_3(t)$. Hence, there are three blocks to calculate the three positions. Each dynamic block's inputs are $\boldsymbol{a}(t)$ and $\boldsymbol{a}_N(t)$ while the single outputs are the positions. These positions feed the coherent dynamic block (three of them shown) to solve the dynamic equation in equation (3.1).

We need to perform the coherent dynamics of c_g and c_e for three different occasions. The first (left down) is the $\pi/2$ splitter induced by a $\pi/2$ optical pulse. The block has inputs such as

- $\Omega_1(t), \Omega_2(t)$: The time dependent optical pulses that drives the coherent dynamics in equation (3.1).
- c_g0, c_e0: the initial conditions of the dynamic variables when the relevant optical pulses (Ω_1, Ω_2) are enabled.

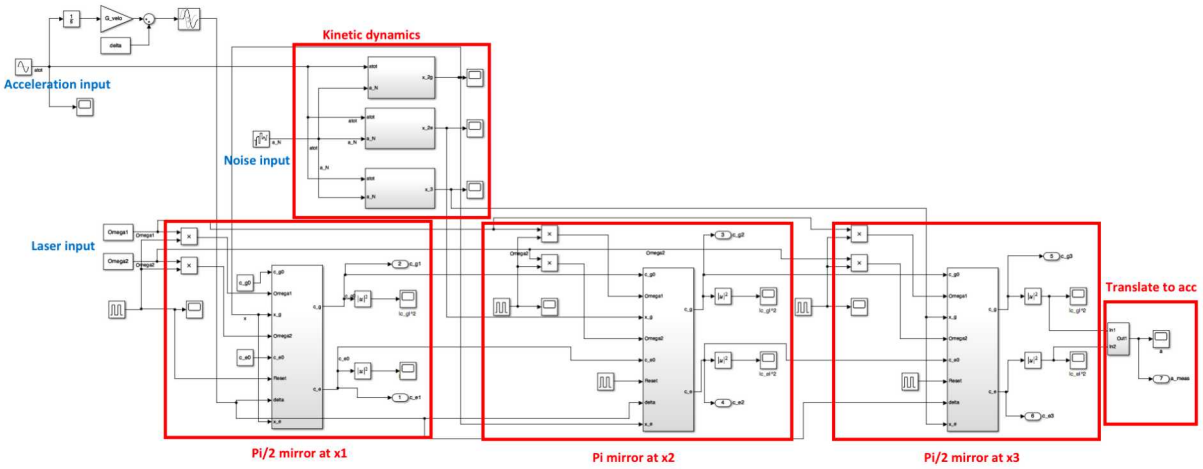

Figure 3.1: Simulink block of the atom interferometer accelerometer

- x_g, x_e: the (time-varying) real time position of the ground and the excited states, at the moment when Ω_1, Ω_2 drive the dynamics. Note that the position $x_{e,g}$ feeding into the dynamics in equation (3.1) is indeed time-varying since the positions are indeed dynamically solved from the aforementioned dynamic simulink block. We thus perform a realistic simulation.

- Reset: this is the trigger to reset the integrator's initial condition. When '*enabled*' by a rising signal, the internal integrator resets the initial condition to the *current* c_g, c_e that feeds the block right at that moment.

- δ: we control the system dynamics through the input parameter δ. The left upper block is one of the possible feed-forward mechanism to control δ. The current built-in one changes δ depending on the measured velocity from another (external) sensor.

The outputs $c_g(t), c_e(t)$ of this block are used as the input initial conditions for the following block.

Once the coherent dynamics are solved for the $\pi/2$ splitting pulse at the position $\boldsymbol{x}_1$, the outputs $c_g(t_1), c_e(t_1)$ are produced. Until t_2, the state does not change (except for the free phase rotation, which we do not count since we are solving $\tilde{c}_g, \tilde{c}_e$). Then, we perform the coherent 'mirror' dynamic simulations for the wave function in state $|e, \boldsymbol{p}_0 + \hbar \boldsymbol{k}_{\text{eff}}\rangle$. For the dynamic block solving the 'pi mirror at x2', the pulses $\Omega_1(t), \Omega_2(t)$ starts at time $t = t_2$, lasting for π pulse duration (π/D'). The initial condition needs reset just before $t = t_2$ through the Reset port, and the integrator starts integrating with the initial condition obtained from the dynamic block for the $\pi/2$ splitter at x1. Note that we feed the position information of both x_{2e} and x_{2g} from the kinetic block above.

The output $c_e(t_2), c_g(t_2)$ from the block 'pi mirror at x2' feed the final interferometer block called 'pi/2 splitter at x3'. The optical signals Ω_1, Ω_2 are enabled at time $t = t_2$ for a duration of $\pi/2$ pulse. This last block produces the outputs $|c_g|^2$ and $|c_e|^2$. For this block, we feed the position x_3 from the kinetic block above. Finally, there is a mathematical block to convert the populations into the measured accelerator.

3.4 Numerical simulation demo

We use the following 'sys-param.m' file for initializing the system parameters.

```
% Simulation parameters

c = 299792458;                          % speed of light in vacuum (m/s)

delta = 2*pi*22e3;                      % Detuning << Omega_eff
Delta = 2*pi*1e9;                       % Detuning, quite large
Omega_eff = 2*pi*250e3;                 % Effective Raman angular frequency
Omega1 = sqrt(Omega_eff*Delta/2);       % Omega_eff = 2*Omega1*Omega2/Delta
Omega2 = Omega1;                        % Usually setting Omega1 = Omega2

lambda1 = 780e-9;
lambda2 = 780e-9;

k1 = 2*pi/lambda1;
k2 = 2*pi/lambda2;

keff = k1 + k2;

c_g0 = 1;                               % Initial population in ground state
c_e0 = 0;                               % Initial population in excited state
x = 0;                                  % Initial position (m)

TT = 70e-6;                             % Cycling period of single acceleration measureme

% Acceleration input parameters (sinusoidal) (acceleration applied, to be
% measured)

atot_amplitude = 10;                    % Sinusoidal amplitude
atot_bias = 0;                          % DC offset
atot_freq = 0.0001*2*pi/TT;               % Frequency in rad/sec
atot_phase_delay = pi/2;                  % Phase delay (radian) of the acceleration app


p_aN = 0;                               % Noise power
M = 86.909187/6.022e23*1e-3;            % Rb87 single atom weight (Kg)
p0 = 0;                                 % Initial momentum of the atom
hbar = 6.626e-34/(2*pi);


D = (Omega2^2 - Omega1^2)/Delta + delta;
Dp = sqrt(D^2 + 4*Omega1^2*Omega2^2/(Delta^2));
T_pi = pi/(Dp);
T_half_pi = T_pi/2;
```

```
G_velo = 0;                          % Feedforward gain
control_delay = 1e-9;                   % Feedforward control delay
%---------------------------
```

Note that according to the equation (2.35), the dynamic range of the measurable acceleration is limited to

$$a_{\max} = \frac{\pi}{T^2 k_{\text{eff}}}, \tag{3.11}$$

which is 39.8 m/s^2 in our case.

3.4.1 Scanning input acceleration

Figure 3.2 shows the simulation result of the atom interference accelerometer. Obviously, the arc-tangential function in equation (2.35) must be periodic with respect to the population ratio, which implies the periodic output with respect to the input acceleration. As expected, the dynamic range of the accelerometer is 0 to approximately 40 m/s, where for large input values the measured acceleration exhibits saturated nonlinear response. This nonlinear response is very clearly seen in the figure below. The solid curve is the measured accelerations while the red dotted line is a linear (guiding) line to compare. Certainly larger input values, the response becomes nonlinear. Moreover, there is a non-zero off-set translation in the X-axis. Later we will show that this off-set depends on the value of δ.

The real instrument, therefore, must use a look-up table to translate the measured acceleration values to map to the real value using the benchmarking curve as above figure. Moreover, the sign of the acceleration must also be determined through an external input, such as an additional external co-sensor that is capable of differentiating the sign of the acceleration.

3.4.2 Scanning the cycling period T

We then scan the cycling time $T = t_2 - t_1 = t_3 - t_2$. The results are shown in figure 3.3. The input acceleration to be measured is 10 m/s^2 in all cases. When T is small, the measurement is inaccurate since the π pulse duration (2 μsec) is non-negligible for short T. This causes a very large error. Then, if T is larger than 50 μs, the measurement starts agreeing with the input acceleration until T reaches approximately 130 μm. Above this value, the measurement suddenly drops down. This is consistant with the criterion in equation (3.11) where a large T will reduce the maximum measurable acceleration.

The same figure also shows the periodic change of the population in the excited and the ground states at the end $t = t_3$. The change of population is very well expected as T varies (see equation (2.35)). Also shown is the fact that the sum of the two populations is always unity.

3.4.3 Scanning δ

We then scan δ for a fixed input acceleration. Figure 3.4 shows the results. The accurate measurement occurs with $\delta = 22$ kHz, for both inputs of $a = 5$ m/s^2 and $a = 10$ m/s^2. As one can see, the measurement is quite sensitive with respect to the value of δ. Therefore, it is important to set the correct δ value.

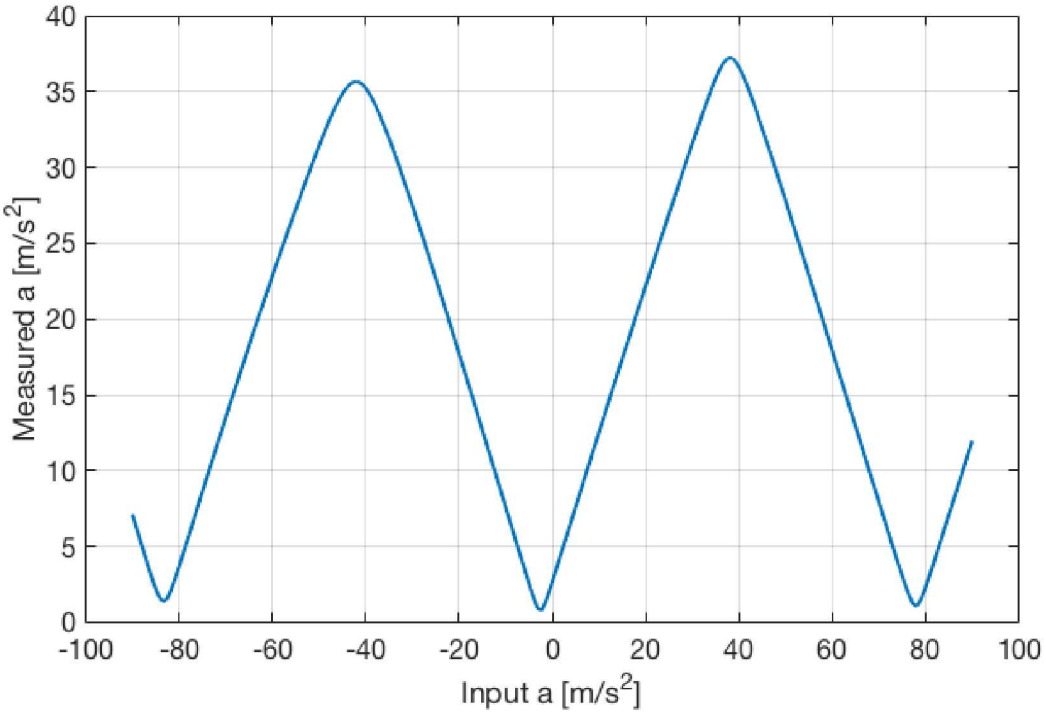

(a) Large range of a

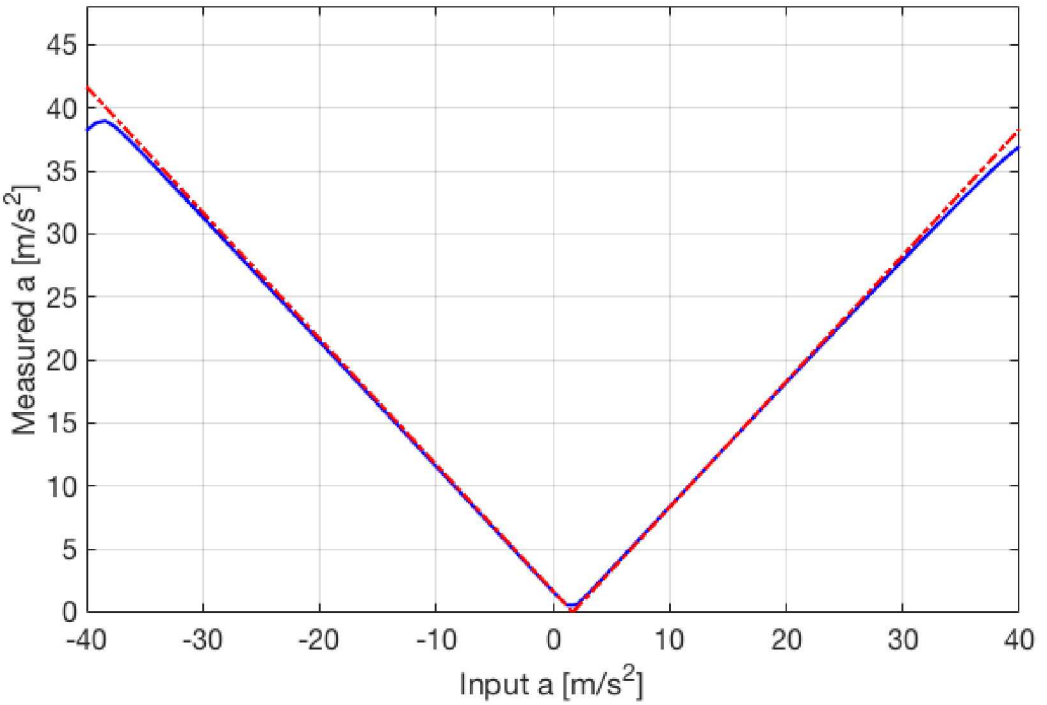

(b) Small range of a

Figure 3.2: Simulation demo for various input acceleration, varying between ± 90 m/s^2 (above), and between ± 40 m/s^2 (below). For the figure below, the linear guiding plot (red dotted) is drawn together to show the linearity of the system response.

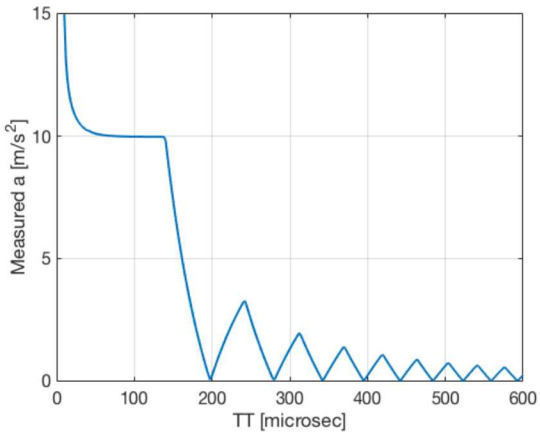

(a) Measured a

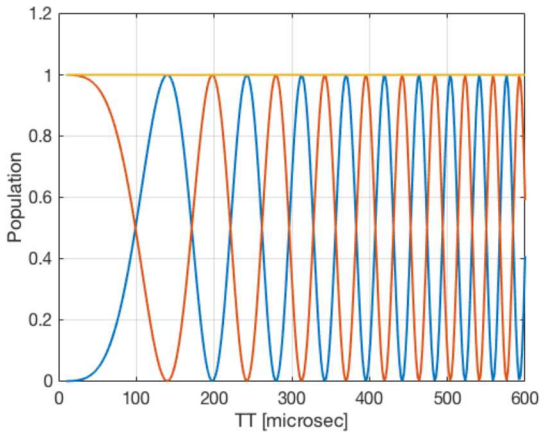

(b) Corresponding excited state population $|c_e(t_3)|^2$

Figure 3.3: Simulation demo for varying $T = t_2 - t_1 = t_3 - t_2$. The input acceleration is 10 m/s^2. Also shown are the populations in the excited state (blue) and the ground state (red), as well as the sum of the two (yellow).

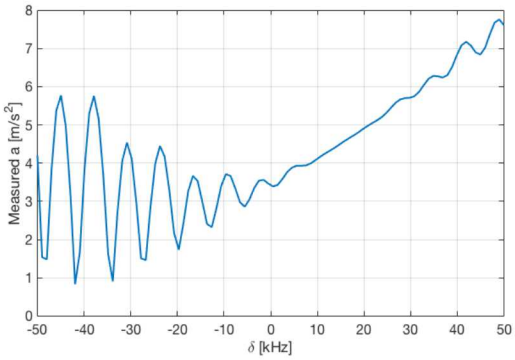

(a) Input $a = 5$ m/s^2

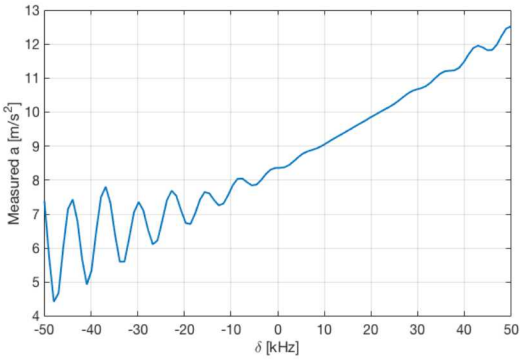

(b) Input $a = 10$ m/s^2

Figure 3.4: Simulation demo for varying δ. Two cases for different input acceleration $a = 5$ m/s^2 (above) and $a = 10$ m/s^2 (below) are shown.

4 Noise canceling schemes

We are interested in canceling out the unwanted fast changing acceleration noise, whose characteristic frequency (central frequency) is higher than the inverse of the single operation time (i.e., $f_0 > 1/(3T)$ where f_0 is the center frequency of the acceleration noise) and $3T$ is the single-cycle AI acceleration measurement process period). Several potential mitigations can be procured as follows.

4.1 Impact of the fast acceleration noise and mitigation

Let us first understand how those fast acceleration noise can affect the measurements. The four position parameters are given as

$$\begin{aligned} x_{2g} &= x_1 + \int_0^T \mathrm{d}t' \left[v_0 + \int_0^{t'} \mathrm{d}t (a_m(t) + a_N(t)) \right], \\ x_{2e} &= x_1 + \int_0^T \mathrm{d}t' \left[v_0 + \frac{\hbar k_{\mathrm{eff}}}{M} + \int_0^{t'} \mathrm{d}t (a_m(t) + a_N(t)) \right], \\ x_3 &= x_1 + \int_0^{2T} \mathrm{d}t' \left[v_0 + \int_0^{t'} \mathrm{d}t (a_m(t) + a_N(t)) \right] + \int_0^T \mathrm{d}t' \frac{\hbar k_{\mathrm{eff}}}{M}. \end{aligned} \tag{4.1}$$

Here, $a_m(t)$ is the acceleration to be measured, $a_N(t)$ is the unwanted fast changing noise, v_0 is the initial speed. Let us assume that $a_m(t)$ is sufficiently slow over $2T$ period. We assume $a_m(t) \approx a_m$, a constant. Then, the above reduces to

$$\begin{aligned} x_{2g} &= x_1 + v_0 T + a_m \frac{T^2}{2} + \int_0^T \mathrm{d}t' v_N(t') = \bar{x}_{2g} + \int_0^T \mathrm{d}t' v_N(t'), \\ x_{2e} &= x_1 + v_0 T + \frac{\hbar k_{\mathrm{eff}}}{M} T + a_m \frac{T^2}{2} + \int_0^T \mathrm{d}t' v_N(t') = \bar{x}_{2e} + \int_0^T \mathrm{d}t' v_N(t'), \\ x_3 &= x_1 + 2v_0 T + \frac{\hbar k_{\mathrm{eff}}}{M} T + 2a_m T^2 + \int_0^{2T} \mathrm{d}t' v_N(t') = \bar{x}_3 + \int_0^{2T} \mathrm{d}t' v_N(t'), \end{aligned} \tag{4.2}$$

where $v_N(t') = \int_0^{t'} a_N(t)\mathrm{d}t$. Each of the position has an extra term in the last (the time integral of $v_N(t')$), and the positions deviate from the noiseless formula $\bar{x}_n$.

Let us focus on the main differential equation in equations (2.13):

$$\begin{aligned} \dot{\tilde{c}}_g &= i\frac{|\Omega_1|^2}{\Delta}\tilde{c}_g + i\frac{\Omega_1 \Omega_2^*}{\Delta}\tilde{c}_e \mathrm{e}^{i(\boldsymbol{k}_2 \cdot \boldsymbol{x}_e - \boldsymbol{k}_1 \cdot \boldsymbol{x}_g + \delta t)}, \\ \dot{\tilde{c}}_e &= i\frac{\Omega_1^* \Omega_2}{\Delta}\mathrm{e}^{i(\boldsymbol{k}_1 \cdot \boldsymbol{x}_g - \boldsymbol{k}_2 \cdot \boldsymbol{x}_e - \delta t)}\tilde{c}_g + i\frac{|\Omega_2|^2}{\Delta}\tilde{c}_e. \end{aligned} \tag{4.3}$$

The impact of the acceleration noise appears in the phase $\boldsymbol{k}_2 \cdot \boldsymbol{x}_e - \boldsymbol{k}_1 \cdot \boldsymbol{x}_g$, which in one dimension with $\boldsymbol{k}_2 = -\boldsymbol{k}_1$ is given as $-k_1(x_e + x_g)$. For the first $\pi/2$ pulse, the effect of the acceleration noise is not significant ($t_1 = 0$). But, for the π pulse at $t_2 = T$, the noise is accumulated and certainly appears in the phase such that

$$-k_1(x_{2e} + x_{2g}) + \delta T = -k_1(\bar{x}_{2e} + \bar{x}_{2g}) - 2k_1 \int_0^T v_N(t')\mathrm{d}t' + \delta T. \tag{4.4}$$

In fact, one can adjust δ to cancel out the effect of the acceleration noise as follows. Set $\delta = \bar{\delta} + \Delta\delta_2$ where $\bar{\delta}$ is the nominal set δ. To cancel the noise term, we assign

$$\Delta\delta_2 = \frac{2k_1}{T}\int_0^T v_N(t')\mathrm{d}t'. \tag{4.5}$$

This will cancel out the acceleration noise, and make the phase term to be $-k_1(\bar{x}_{2e} + \bar{x}_{2g}) + \bar{\delta}T$. Similarly at time $t_3 = 2T$, one also assigns the adjusting $\Delta\delta_3$ to be

$$\Delta\delta_3 = \frac{k_1}{T}\int_0^{2T} v_N(t')\mathrm{d}t'. \tag{4.6}$$

This cancels out the acceleration noise in the phase term for the second $\pi/2$ pulse at time $t_2 = 2T$. This way, one can still obtain

$$x_1 - x_{2g} - x_{2e} + x_3 = \bar{x}_1 - \bar{x}_{2g} - \bar{x}_{2e} + \bar{x}_3 = a_m T^2, \tag{4.7}$$

where $\bar{x}_1 = x_1$. Therefore, the population-induced acceleration measurement will yield $|a_m|$ as we intend through the equation (2.32).

4.2 Feedforward scheme based on a fast, but rough, cosensor

The only technical problem is how to obtain $v_N(t') = \int_0^{t'} a_N(t)\mathrm{d}t$. One way is to use a fast auxiliary accelerometer with a high-pass filter. Let us denote the entire acceleration as $a_m(t) + a_N(t)$ where the varying speed of $a_m(t)$ is slower than $1/(3T)$ (where $3T$ is the single-cycle AI acceleration measurement time) while $a_N(t)$ is faster than $1/(3T)$. Then, we can approximately separate

$$F_{HP}(j\omega)(a_m(j\omega) + a_N(j\omega)) = \frac{j\omega/\omega_f}{1 + j\omega/\omega_f}(a_m(j\omega) + a_N(j\omega)) \approx a_N(j\omega), \quad \omega \gg \omega_f \tag{4.8}$$

for high frequency $\omega > \omega_f$ with the filter cut-off frequency ω_f. Here F_{HP} is the transfer function of a high pass filter, for which we used the first-order high pass filter in this case. One has a full freedom to choose whichever filter suits best for the purpose of separating a_N from $a_m + a_N$.

We tested this feedforward scheme. We simulated the frequency response of the noise input to the measured acceleration. For this, we set $a_m = 10$ m/s^2. The noise a_N is assumed to be a sinusoidal with am amplitude of 5 m/s^2 and a frequency f_N. We scanned f_N from $1/(3T)$ to $10^5/(3T)$, and measured the error of the measured acceleration compared to the noiseless case. Note that this method is equivalent to measure the output acceleration spectrum when the input is a white noise over the frequency range of interest.

Figure 4.1 shows the result. The first is the ideal filter case where we assume that $a_N(t)$ is perfectly separated (figure 4.1 (a)). The detected noise has some complex shape, which may be affected by the details in the differential equation solver of the Simulink as well as the system's peculiarity. Nevertheless, we could successfully suppress the noise well below 0.001% of the correct acceleration of 10 m/s^2. This shows that the feedforward scheme is quite successful. Note, however, that this case used an ideal filter that perfectly separated $a_N(t)$. This, however, is unrealistic since no accelerator can separate a_N from

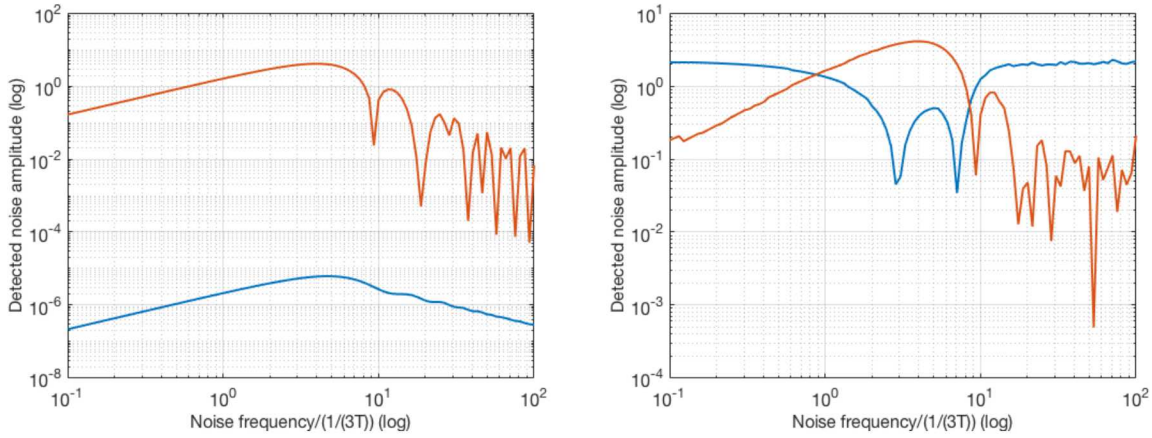

(a) Ideal filter (b) Realistic filter

Figure 4.1: Noise spectrum in the measured acceleration. Above: using an ideal filter to separate a_N perfectly, below: using a realistic high pass filter to separate a_N. The blue and yello curves represent the feedforward-compensated and the non-compensated (no feedforward compensation), respectively. The input noise is white-noise equivalent.

$a_{\text{tot}} = a_m + a_N$ if the noise frequency is near zero.

We then adopted a realistic high-pass filter with a transfer function of $s/(s + fc)$ with a cut-off frequency f_c. For this particular example, we used $fc = 5/(3T)$. The result is shown in figure 4.1 (b). This is quite a realistic simulation where we use a fast rough auxiliary accelerometer, through a high-pass filter to separate the high-frequency component of a_N to use in the feedforward compensation scheme. Consequently, the noise that has low frequency cannot be separated, and directly affects the measured acceleration. The spectrum surely shows that the low-frequency noise affects the result significantly, while there is a band of noise spectrum that is efficiently suppressed through the feedforward scheme. On the other hand, very high frequency noises are not amplified through this crude high-pass filter scheme. It is thought to be that the compensation is out of phase, and leaves some nonzero residuals after the compensation. This example shows the need for a good high-pass filter and phase adjustment in the feedforward compensation scheme.

4.3 Feedback scheme

Alternatively, one can use the previously measured a_m from AI, and use the formula $a_{\text{tot}}(n) - a_m(n-1) = (a_m(n) + a_N(n)) - a_m(n-1) \approx a_N(n)$ where n is the discrete time index. Compared to the above method where an auxiliary fast accelerometer is used, this method has an advantage to eliminate the need for such high-speed extra accelerometer. More importantly, this method is expected to be much more accurate than the above since the measured a_m from the AI accelerometer is expected to be much more accurate than the fast, but crude auxiliary accelerometer. However, in this method, one would make sure that the measurement cycle frequency $1/3T$ is much faster than the characteristic varying speed of a_m so that one guarantees $a_m(n-1) \approx a_m(n)$.

4.4 Study on noise output spectrum

In this section we will study the effect of the noise to the output of the AI accelerometer. We assume a single sinusoidal noise, on top of the acceleration to be measured with a certain frequency with a certain amplitude and a certain phase. Then, we will scan all the three parameters: frequency, amplitude, and phase. This way, we will obtain the numerical noise output spectrum.

First of all, the noise output is defined to be the difference between the measured acceleration while the noise sinusoidal signal is absent and the one without the noise signal.

In all analysis, we assume the same simulation parameters as the previous section unless specified. The acceleration to be measured is set to 10 m/s^2.

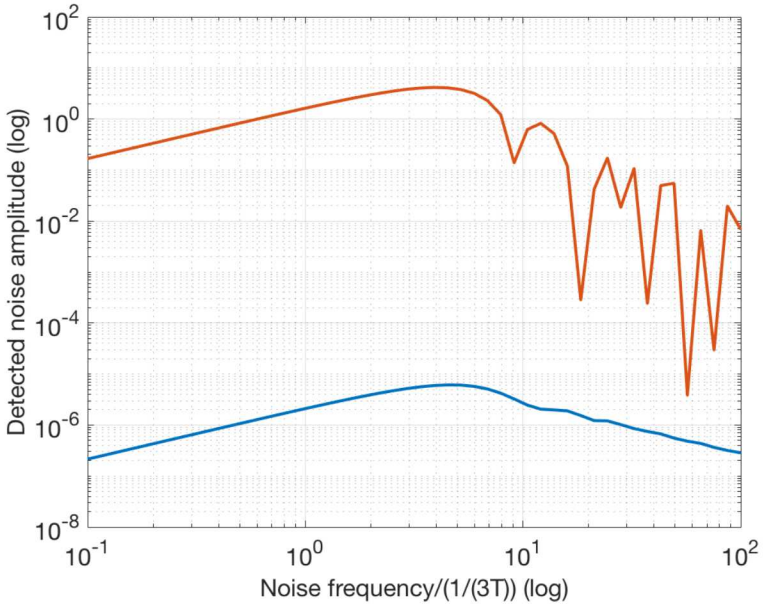

Figure 4.2: The output noise spectrum (red curve) for the input sinusoidal noise with various frequency while fixing the noise amplitude as 5 m/s^2 and the noise phase as zero for all frequencies. Also shown is the noise-cancelled output by adopting the ideal feedforward scheme (blue).

We first study the effect of the noise frequency while fixing the noise amplitude to be 5 m/s^2 and the phase of the noise to be zero. The result is shown in figure 4.2. In this particular case, the most severe noise occurs at around a frequency of $1/T$. This is understandable since the three mirror/splitter pulses occurs with a time interval of T, and every time the pulse is applied, the noise constructively affects the position of the test mass.

It is expected that the output noise will be affected by the phase of the sinusoidal noise. We simulated different spectra with a three different fixed noise phase (see the figure 4.3). Obviously the spectra are all different for different values of the noise phases. Only thing common among the three cases is the fact that high frequency noise would not affect significantly the performance of the AI accelerometer. This is because the high frequency noise becomes diminished by averaging out over the pulse duration. Particularly when the noise frequency is comparable to or higher than the inverse of the pulse duration, the noise would not appear in the measured output.

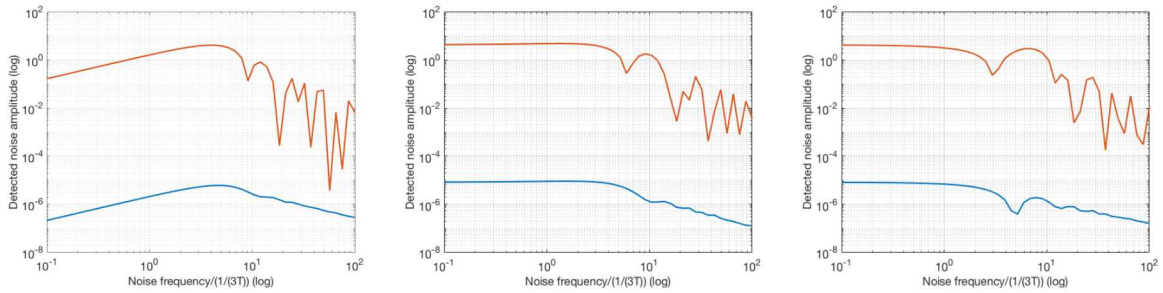

(a) Noise phase = 0 rad (b) Noise phase = $\pi/3$ rad (c) Noise phase = $2\pi/3$ rad

Figure 4.3: The output noise spectra (red curve) for the input sinusoidal noise with various frequency while fixing the noise amplitude as 5 m/s^2. Three different cases with noise phases of 0 (left), $\pi/3$ (center), and $2\pi/3$ (right) rad. For each case, the noise phase is fixed for all frequencies. Also shown is the noise-cancelled output by adopting the ideal feedforward scheme (blue).

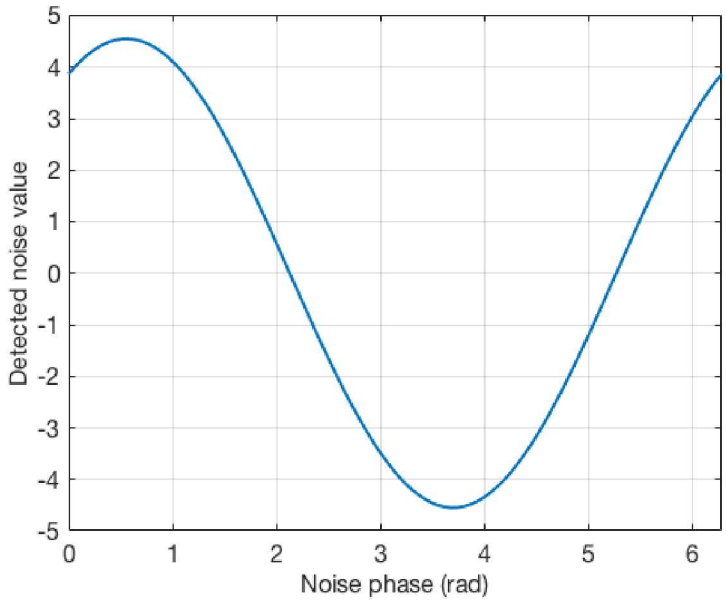

Figure 4.4: The output noise for the input sinusoidal noise depending on the noise phase, while fixing the noise amplitude as 5 m/s^2 and the noise frequency to be $1/T$.

To see the impact of the noise phase more precisely, we fix now the noise frequency to be $1/T$, and sweep only the noise phase. The result is shown in figure 4.4. It is interesting to see that the output value change due to the input noise becomes both negative and positive values, depending on the phase of the noise, which is indeed well expected. It is also interesting that there are noise phase values that incur zero disturbance to the output, which is perhaps due to the destructive net impact on the output value while affecting the three mirror/splitter pulses.

With all these, it is now clear that a root-mean-squared noise output is necessary to understand the output noise spectra that is agnostic to (or averaged over) the noise phase. The mere output noise average over different phases is not sufficient since it will simply become zero as seen from the figure 4.4. The r.m.s. noise output is calculated as squaring

the noise output (difference between the output with and without the noise), averaging this quantities over all phase values in $[0, 2\pi]$, and taking the square root of the average. The result is shown in figure 4.5.

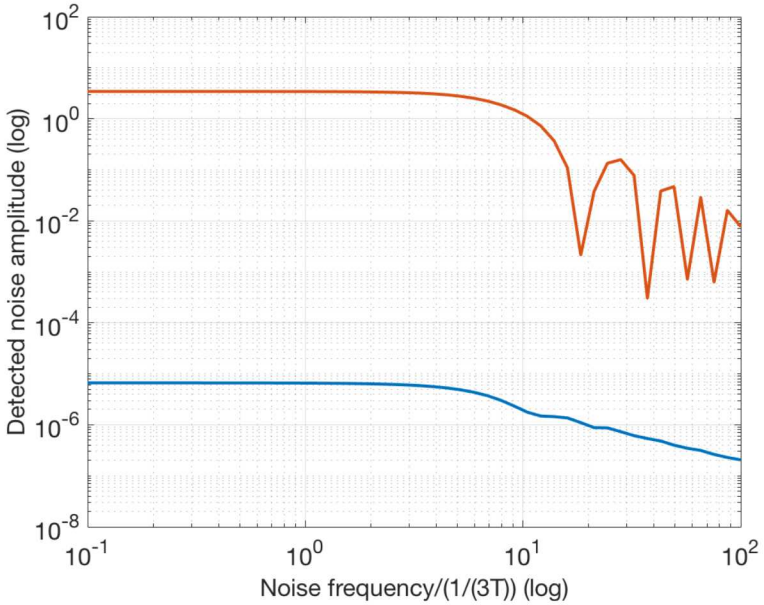

Figure 4.5: The r.m.s. (over noise phase) output noise spectrum (red curve) for the input sinusoidal noise with various frequency while fixing the noise amplitude as 5 m/s^2. Also shown is the noise-cancelled output by adopting the ideal feedforward scheme (blue).

The r.m.s. (over phase noise) noise output spectrum shows rather a flat spectrum below frequency $1/T$, while the impact of the noise gradually reduces beyond frequency $1/T$, with the same reason for diminishing as above. This indeed shows that the impact of the noise below frequency $1/T$ is equally large, regardless of the noise frequencies. In other words, the AI accelerometer is greatly affected by low frequency noise source with frequencies comparable to the cycling time and below.

It is also quite remarkable that the ideal feedforward noise canceling scheme using the cosensor is quite effective in all cases with various different noise parameters. Particularly the final r.m.s. output noise spectrum shows that the feedforward noise canceling reduced the noise in all frequencies by nearly three orders of magnitude.

Finally, we study the impact of the noise amplitude to the output acceleration measurement. For this, we fixed the noise frequency to $1/T$, and the noise amplitude to zero. We then sweep the noise amplitude between 0 m/s^2 and 5 m/s^2 (recall that the acceleration to be measured is 10 m/s^2). The normalized output noise is obtained by dividing the output noise (difference between the measured acceleration with and without the noise) by the input noise amplitude. The result is shown in figure 4.6. Clearly, the output noise amplitude is linear to the input noise amplitude, and thus the normalized output noise is a constant over various input noise amplitudes. This shows that the input/output noise relation is indeed a linear relation.

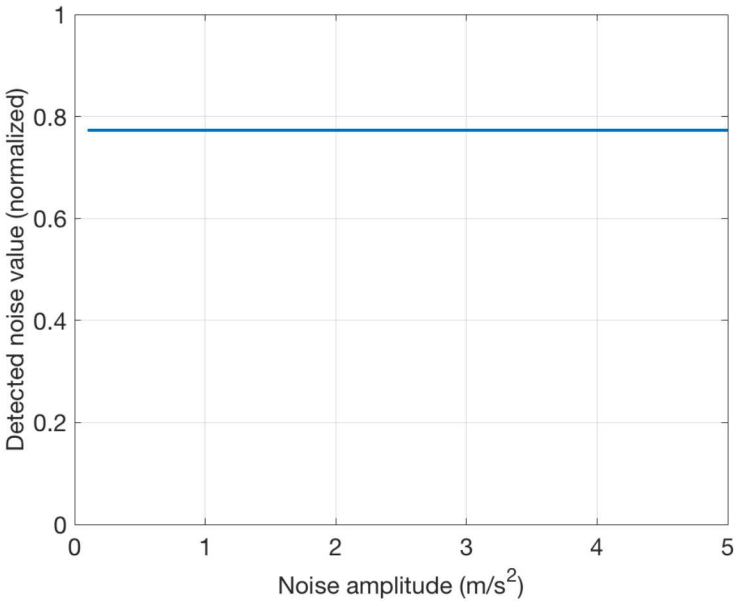

Figure 4.6: The normalized output noise value for the input sinusoidal noise with a frequency $1/T$ while varying the noise amplitude.

5 Effect of atom movement during Raman pulses

The simulink faithfully models the details of the atoms and their quantum behaviors. It is noteworthy that the atoms actually move during the short Raman pulse durations. Then, the assumption of the instantaneous beam splitters and the mirror is no longer true. The parameter $\Delta_{kx} = \boldsymbol{k}_1\boldsymbol{x}_g - \boldsymbol{k}_2\boldsymbol{x}_e$ is no longer a constant during the Raman pulse since both $\boldsymbol{x}_{g,e}$ changes due to the atom velocity, which is affected by the applied acceleration.

5.1 Differential equations of moving atoms

The differential equations in equations (3.1) are indeed coupled to the dynamics of the atom positions given through

$$\begin{aligned}\dot{x}_e(t) &= v_e(t),\\ \dot{x}_g(t) &= v_g(t),\\ \dot{v}_e(t) &= a,\\ \dot{v}_e(t) &= a,\end{aligned} \tag{5.1}$$

with the initial conditions for $t = t_1$ for the first Raman $\pi/2$-pulse (see figure 2.2)

$$\begin{aligned}x_g(t_1) &= x_e(t_1) = x_1,\\ v_g(t_1) &= v_0,\\ v_e(t_1) &= v_0 + \frac{\hbar k_{\text{eff}}}{M},\end{aligned} \tag{5.2}$$

and for $t = t_2$ for the Raman π-pulse:

$$\begin{aligned} x_g(t_2) &= x_1 + v_0(t_2 - t_1) + \frac{1}{2}a(t_2 - t_1)^2, \\ x_e(t_2) &= x_1 + v_0(t_2 - t_1) + \frac{1}{2}a(t_2 - t_1)^2 + \frac{\hbar k_{\text{eff}}}{M}(t_2 - t_1), \\ v_g(t_2) &= v_0 + a(t_2 - t_1), \\ v_e(t_2) &= v_0 + a(t_2 - t_1) + \frac{\hbar k_{\text{eff}}}{M}, \end{aligned} \tag{5.3}$$

and also for $t = t_3$ for the last Raman $\pi/2$ pulse, we have

$$\begin{aligned} x_g(t_3) = x_e(t_3) &= x_1 + v_0(t_3 - t_1) + \frac{1}{2}a(t_3 - t_1)^2 + \frac{\hbar k_{\text{eff}}}{M}(t_2 - t_1), \\ v_g(t_3) &= v_0 + a(t_3 - t_1), \\ v_e(t_3) &= v_0 + a(t_3 - t_1) + \frac{\hbar k_{\text{eff}}}{M}. \end{aligned} \tag{5.4}$$

with the understanding that $t_2 - t_1 = t_3 - t_2 = T$.

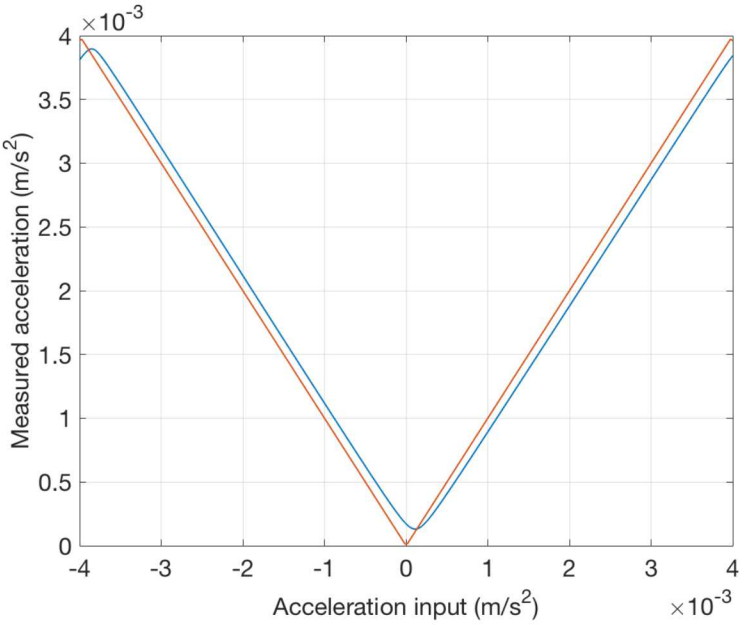

Figure 5.1: Comparison of the input-output relation for moving atoms (blue) and frozen atoms (red) during the Raman pulses.

5.2 Effect on acceleration measurement

To see things very clearly, we compare two cases. The first lets the atoms change their positions $\boldsymbol{x}_{g,e}$ during the Raman pulse while the second 'freezes' the atoms during the Raman pulse so that Δ_{kx} is a constant. Figure 5.1 shows the clear difference. When the atoms are (artificially) frozen during the Raman pulses, the measured acceleration faithfully represent the input acceleration. However, when the atoms are moving during the Raman pulses, which is the actual truthful description of the physics, the measured

acceleration starts deviating from the input acceleration. We note that this particular case has the parameter value $TT = t_2 - t_1 = 7$ ms[1]. From this, it is expected that, if the Rabi oscillation frequency $\Omega_{\text{eff}} = 2\Omega_1\Omega_2/\Delta$ becomes large, such undesired effect of the moving atoms will reduce.

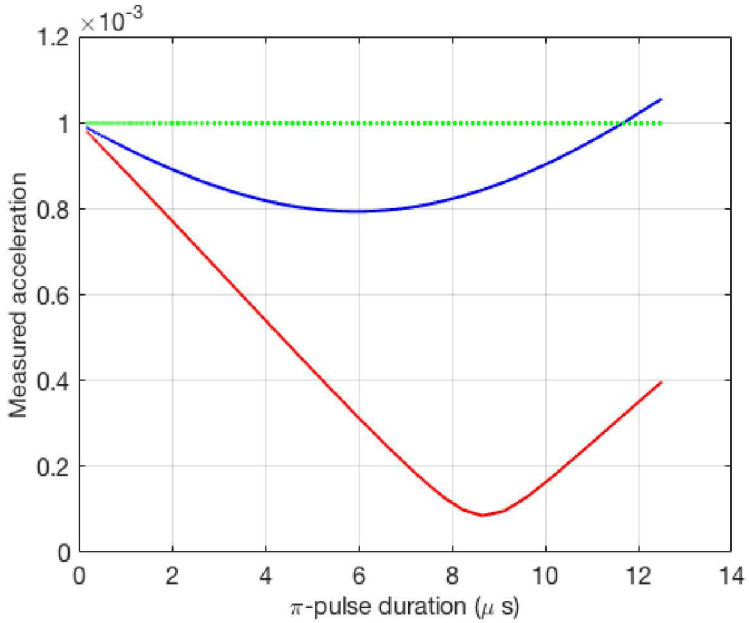

Figure 5.2: Measured acceleration output as a function of the Raman π-pulse duration for moving atoms during ther Raman pulse. Blue: when the initial velocity was zero, red: when the initial velocity was 0.005 m/s. Green dots indicates the ideal measurement.

Figure 5.2 shows the relation between the measured output acceleration and the Raman π-pulse duration. As expected, shorter π-pulse duration approaches the desired output measurement. We actually varied the Rabi frequency Ω_{eff} between $2\pi \times$ [30 kHz, 3 MHz], which varied the Raman π-pulse duration from 12.3 μs to 0.125 μs. The nominal π-pulse duration for all previous examples was 2 μs, corresponding to the Rabi frequency $\Omega_{\text{eff}} = 2\pi \times (250$ kHz). The curve is not simple. When the π-pulse duration is small, the measured acceleration reduces as the pulse duration increases. However, it changes the sign of tangent around at 6 μs, and starts increasing. This behavior is understandable considering that Δ_{kx} enters as a phase, and the periodic behavior is expected.

We also note that the trend between the input and the measured output depends on the atom velocity at the moment of the Raman pulse application. It is expected that when the atom velocity is large, the measurement would be more affected. Figure 5.2 shows the comparison between the case of zero initial atom velocity and the initial atom velocity of 0.005 m/s. Obviously the case of $v_0 = 0.005$ m/s deviates much more from the ideal measurement. In both cases, the measurement converges to the input acceleration for extremely short π-pulse duration.

Then, the next question is the measurement dependence on the initial atom velocity since the degree of atom movement during the Raman pulse not only depends on the

[1]All previous simulation results used the value $TT = 70$ μs. Hence, the maximum measurable acceleration in previous examples was 40 m/s^2, while changing $TT = 7$ ms reduces the maximum measurable acceleration to be only 4×10^{-3} m/s^2. See equation (3.11).

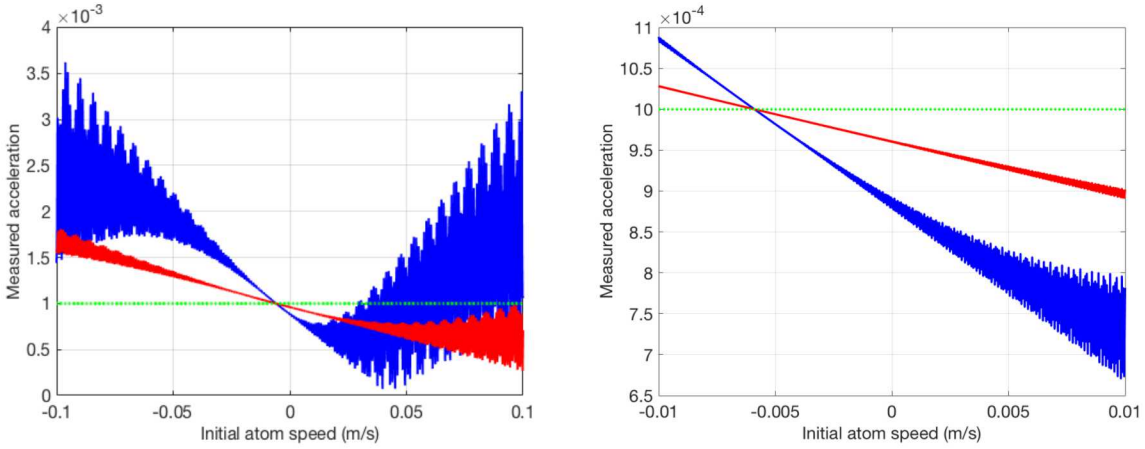

(a) Larger initial velocity domain (b) Smaller initial velocity domain

Figure 5.3: Measured acceleration output as a function of the initial atom velocity for moving atoms during ther Raman pulse. Blue: with $\Omega_{\text{eff}} = 2\pi \times 250$ kHz, red: with $\Omega_{\text{eff}} = 2\pi \times 750$ kHz. Green dots indicates the ideal measurement.

Raman pulse duration, but also depends on the instantaneous velocity at the moment of the Raman pulses. Figure 5.3 shows the result. When the Raman π-pulse duration was 2 μs (i.e., $\Omega_{\text{eff}} = 2\pi \times (250$ kHz)), the blue curve shows significant dependence of the measured acceleration on the initial atom velocity. For example, if the atom temperature is 50 μK, the thermal velocity (r.m.s.) is $\sqrt{k_B T_e/m} = 0.07$ m/s where k_B is the Boltzmann constant and T_e is the temperature. Then, the measurement would be very seriously affected by long Raman pulses. To mitigate the impact, one must reduce the Raman pulse duration, i.e., increase the Raman pulse's optical power significantly. The figure also shows the case for the Raman π-pulse duration of 0.67 μs (i.e., $\Omega_{\text{eff}} = 2\pi \times (750$ kHz)). The impact of the initial atom speed is significantly reduced.

All of these indicate the significance of the movement of the atoms during the application of the Raman pulses. Ideally one would want the atoms to be 'frozen' during the Raman pulses. Unfortunately, however, the atoms move due to both the initial velocity and the applied acceleration, and such atom movement cannot be avoided. The atom movement will eventually affect the accuracy of the acceleration measurement. The obvious mitigation is by reducing the Raman pulse duration, which requires increasing the Rabi oscillation frequency that is proportional to the field amplitude (square-root of the optical power).

5.3 Doppler effect

When the atom moves with a velocity v in the same direction of the incoming light, the light frequency that the atom feels is

$$\omega = \left(1 - \frac{v}{c}\right) \omega_0, \tag{5.5}$$

where ω_0 is the light frequency that a stationary atom (not moving) feels. Hence, the light frequency reduces. Consequently, if the atom moves with $v' = -v$, opposite to the

direction of the incoming light, the light frequency that the atom feels is

$$\omega' = \left(1 - \frac{v'}{c}\right)\omega_0 = \left(1 + \frac{v}{c}\right)\omega_0. \tag{5.6}$$

We are interested in the momentum change from the Doppler effect, which is given through the light dispersion of $k = \omega/c$. Hence, when the atom has a velocity v in the same direction as the incoming light, the momentum of that the atom feels is

$$k = \left(1 - \frac{v}{c}\right)k_0, \tag{5.7}$$

where $k_0 = \omega_0/c$. When, the atom has the opposite direction velocity $v' = -v$, the atom feels

$$k' = \left(1 + \frac{v}{c}\right)k_0. \tag{5.8}$$

From the figure 2.1 (b), when the atom has a velocity v to the right, we need to modify k_1 and k_2 such that

$$k_1 \to \left(1 - \frac{v}{c}\right)k_1, \quad k_2 \to \left(1 + \frac{v}{c}\right)k_2. \tag{5.9}$$

This modification must be made to the model. Note that $v = v(t)$ is indeed the instantaneous velocity that the atom currently possess (at the moment of the Raman pulse).

The effect of the Doppler shift is best seen by calculating the transfer matrix as a function of the initial velocity v_0 and the applied acceleration a, which is considered a constant for now. Then, for each pulse, the parameter

$$\begin{aligned}\Delta_{kx} &= \boldsymbol{k}_1 \cdot \boldsymbol{x}_g - \boldsymbol{k}_2 \cdot \boldsymbol{x}_e = (k_{\text{eff}}/2)(1 - v_g/c)x_g + (k_{\text{eff}}/2)(1 + v_e/c)x_e \\ &= (k_{\text{eff}}/2)(x_g + x_e) + (k_{\text{eff}}/2c)(v_e x_e - v_g x_g).\end{aligned} \tag{5.10}$$

when the photon momentum is collinear with the position vectors. Hence, for the first $\pi/2$ pulse, we have $x_g = x_e = x_1$ and $v_g = v_e = v_0$, and

$$\Delta_{kx}^{(1)} = k_{\text{eff}} x_1, \tag{5.11}$$

which is identical to the case ignoring the Doppler shift. However, for the π pulse, we have $v_{2g} = v_0 + aT$, $v_{2e} = v_0 + \hbar k_{\text{eff}}/M + aT$. Here, $T = t_2 - t_1$. Hence, we obtain

$$\Delta_{kx}^{(2)} = \frac{k_{\text{eff}}}{2}(x_{2e} + x_{2g}) - \frac{\hbar k_{\text{eff}}^2}{2cM}x_{2e} - \frac{k_{\text{eff}}}{2c}(aT + v_0)(x_{2e} - x_{2g}). \tag{5.12}$$

For the second $\pi/2$ pulse, we have $v_{3g} = v_0 + 2aT + \hbar k_{\text{eff}}/M = v_{3e}$, and $x_{3g} = x_{3e}$. Hence, we have

$$\Delta_{kx}^{(3)} = k_{\text{eff}} x_3. \tag{5.13}$$

After all, the impact of the Doppler shift is only in the second pulse dynamics.

The transfer matrix calculation results in the population ratio:

$$\frac{|c_e|^2}{|c_g|^2} = \tan^2\left[\frac{1}{2}(\Delta_{kx}^{(1)} - 2\Delta_{kx}^{(2)} + \Delta_{kx}^{(3)})\right]. \tag{5.14}$$

Therefore, the extra phase due to the Doppler shift is given through the final result:

$$|\boldsymbol{a} - 2\boldsymbol{v} \times \boldsymbol{\Omega}| = \frac{2}{T^2 k_{\text{eff}}} \left[\text{atan} \left| \frac{c_e(t_{\text{read}})}{c_g(t_{\text{read}})} \right| \right] - \frac{\hbar k_{\text{eff}}}{2cMT^2} x_{2e} - \frac{1}{2cT^2}(aT + v_0)(x_{2e} - x_{2g}). \quad (5.15)$$

Note that

$$\begin{aligned} x_{2e} &= x_1 + v_0 T + \frac{\hbar k_{\text{eff}}}{M} T + \frac{a}{2} T^2, \\ x_{2g} &= x_1 + v_0 T + \frac{a}{2} T^2. \end{aligned} \quad (5.16)$$

Therefore, the effect of the Doppler shift is given as an error for the measured acceleration:

$$\Delta a = a_0 - \frac{\hbar k_{\text{eff}}}{cMT} v_0, \quad (5.17)$$

where a_0 is a constant independent of v_0, which is negligible. Note that the error is linear to the initial velocity v_0.

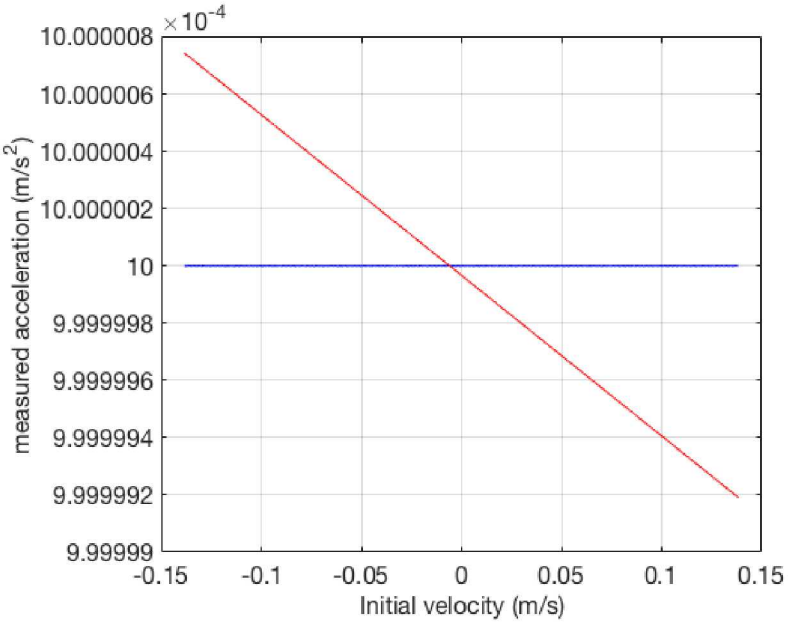

Figure 5.4: Comparison between the measured acceleration depending on the initial velocity, while atoms are frozen during the Raman pulses. With Doppler effect (red), without Doppler effect (blue). For this simulation, we set the applied acceleration of 1×10^{-3} m/s^2, and set $T = 7$ ms and $\Omega_{\text{eff}} = 2\pi \times (750$ kHz).

To separate the effect of the moving atoms while Raman pulse duration (see previous section) and purely the Doppler effect, we first 'freeze' the atom movement while the Raman pulse duration, and compare the measured accelerations with and without the Doppler effect. Figure 5.4 shows the comparison of the two cases. The slope of the measured acceleration against the initial velocity from this detailed calculation (the case with Doppler effect, red curve) is found to be -5.38×10^{-9} s. Let us compare with our analysis above. According to the equation (5.17), the expected slope is $-\hbar k_{\text{eff}}/(cMT) = -5.61 \times 10^{-9}$ s, which is very close to the value of the full numerical simulation. This shows that our analysis, although it only counts the first-order perturbation, is close to

the actual values. Note that the Doppler effect that is 10^{-7} in this thermal initial velocity domain is negligibly small compared to the moving atom effect (see figure 5.3), which is same unity-order error in the same initial velocity domain.

5.4 Initial thermal velocity distribution of many atoms

The AI accelerometer uses an ensemble of cold atoms cooled at a certain low temperature. Naturally the atoms have the dispersive initial velocities in accordance with the Boltzmann distribution for a given temperature. For a $d-$dimensional system, the probability distribution $f(\boldsymbol{v})$ for an atom to have a velocity $\boldsymbol{v}$ is given as

$$f(\boldsymbol{v}) = \left(\frac{2\pi k T_e}{m}\right)^{-d/2} \exp\left[-\frac{|\boldsymbol{v}|^2}{(2kT_e/m)}\right], \tag{5.18}$$

where m is the atom mass, k the Boltzmann constant, and T_e the temperature. The normalization is such that $\int f(\boldsymbol{v}) d^d\boldsymbol{v} = 1$.

Let us combine the effect of the moving atoms while the Raman pulse duration and the Doppler effect and see the net effect of the initial atom velocity. Again, it is highly expected that the effect of moving atoms, which is a 10^7 order-of-magnitude larger effect than the Doppler effect, will be dominant.

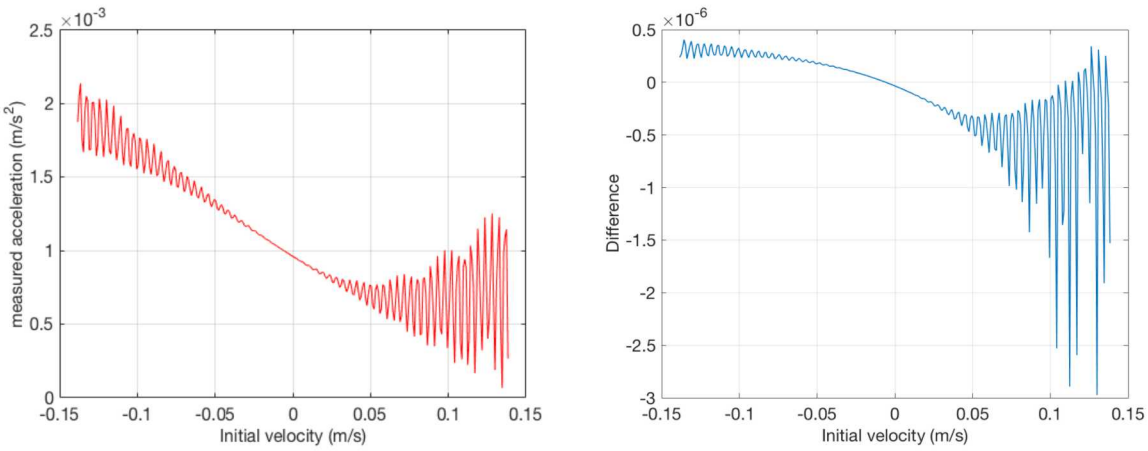

(a) Measured acceleration comparison (b) Difference

Figure 5.5: The measured acceleration under the influence of moving atoms, depending on the initial atom velocity. (a) The combined effect of Doppler and moving atoms during Raman pulses (red), and the effect of moving atoms alone without Doppler (blue), which is not shown due to the complete overlap between the red and the blue curves. (b) The relative difference of the red and the blue curves in (a). We set $\Omega_{\text{eff}} = 2\pi \times (750\ \text{kHz})$.

To see thing clearly, we now turn on both the atom movement during Raman pulses and the Doppler effect. Then, we turn on only the atom movement during Raman pulses and turn off the Doppler effect to see the difference to isolate the Doppler effect alone. Figure 5.5 shows the result. The left graph shows the measured acceleration as a function of the initial velocity when both atom movement during Raman pulses and the Doppler effect are turned on. Due to the negligibly small effect from Doppler, the difference is not clear. Hence, we calculated $(a^{\text{DM}}_{\text{meas}} - a^{\text{M}}_{\text{meas}})/a^{\text{DM}}_{\text{meas}}$ where $a^{\text{DM}}_{\text{meas}}$ is the measured acceleration

when both effects are turned on and $a^{\mathrm{M}}_{\mathrm{meas}}$ is the measured acceleration when only the dominant atom movement is turned on while the Doppler is turned off. As expected, the Doppler effect is 10^{-6} order-of-magnitude smaller than the moving atoms.

One thing remarkable about the Doppler effect shown in the context where the effect of moving atoms during the Raman pulses is turned on, is that the Doppler effect is also wiggly, albeit very small in overall magnitude.

The conclusion so far is that the Doppler effect is quite negligible, compared to the effect of the atom movement during the Raman pulses. Hence, for the higher accuracy, one must increase the Raman pulse intensity to reduce down the Raman pulse duration, and minimize the effect of the atom movement during the short Raman pulses.

5.5 Mitigation of atom movement

The mitigation is quite simple. For this, let us review the differential equation during the Raman pulses (the equations (3.1)):

$$\begin{aligned}\dot{\tilde{c}}_g &= i\frac{|\Omega_1|^2}{\Delta}\tilde{c}_g + i\frac{\Omega_1\Omega_2^*}{\Delta+\delta}\tilde{c}_e \mathrm{e}^{i(\boldsymbol{k}_2\cdot\boldsymbol{x}_e - \boldsymbol{k}_1\cdot\boldsymbol{x}_g+\delta t)},\\ \dot{\tilde{c}}_e &= i\frac{\Omega_1^*\Omega_2}{\Delta}\mathrm{e}^{i(\boldsymbol{k}_1\cdot\boldsymbol{x}_g - \boldsymbol{k}_2\cdot\boldsymbol{x}_e-\delta t)}\tilde{c}_g + i\frac{|\Omega_2|^2}{\Delta+\delta}\tilde{c}_e.\end{aligned} \tag{5.19}$$

One can engineer the instantaneous δ value to mitigate the atom movement that manifest in the phase term $\boldsymbol{k}_2\cdot\boldsymbol{x}_e - \boldsymbol{k}_1\cdot\boldsymbol{x}_g + \delta t$. Note that

$$\boldsymbol{x}_i(t) = \frac{1}{2}\boldsymbol{a}(t-t_0)^2 + \boldsymbol{v}_{i0}(t-t_0) + \boldsymbol{x}_{i0}, \tag{5.20}$$

where $i = e, g$, and t_0 is the starting time stamp for the beginning of the Raman pulse, $\boldsymbol{v}_{i0}$ is the atom velocity at time t_0, and $\boldsymbol{x}_{i0}$ is the atom position at time t_0. Assuming $\boldsymbol{k}_1 = -\boldsymbol{k}_2$ ($k_{\mathrm{eff}} = |\boldsymbol{k}_1 - \boldsymbol{k}_2| = 2|\boldsymbol{k}_1|$), and the atom movements are colinear with respect to $\boldsymbol{k}_1$, we can feedforward $\delta(t)$ to satisfy

$$\delta_m(t) = \frac{k_{\mathrm{eff}}}{2t}[a(t-t_0)^2 + (v_{g0}+v_{e0})(t-t_0)]. \tag{5.21}$$

With this time varying detuning $\delta(t) = \delta_m(t)$, it is straightforward to verify that the phase is now $\boldsymbol{k}_2\cdot\boldsymbol{x}_{e0} - \boldsymbol{k}_1\cdot\boldsymbol{x}_{g0} = -(k_{\mathrm{eff}}/2)(x_{g0}+x_{e0})$, which does not depend on time. With the feedforward $\delta(t) = \delta_m(t)$, the differential equation now turns to

$$\begin{aligned}\dot{\tilde{c}}_g &= i\frac{|\Omega_1|^2}{\Delta}\tilde{c}_g + i\frac{\Omega_1\Omega_2^*}{\Delta+\delta}\tilde{c}_e \mathrm{e}^{i(\boldsymbol{k}_2\cdot\boldsymbol{x}_{e0} - \boldsymbol{k}_1\cdot\boldsymbol{x}_{g0})},\\ \dot{\tilde{c}}_e &= i\frac{\Omega_1^*\Omega_2}{\Delta}\mathrm{e}^{i(\boldsymbol{k}_1\cdot\boldsymbol{x}_{g0} - \boldsymbol{k}_2\cdot\boldsymbol{x}_{e0})}\tilde{c}_g + i\frac{|\Omega_2|^2}{\Delta+\delta}\tilde{c}_e.\end{aligned} \tag{5.22}$$

The atom movement effect is completely canceled by the feedforward $\delta(t) = \delta_m(t)$.

With the feedforward $\delta_m(t)$, we could obtain a very nice result that completely eliminates the effect of the moving atoms during the Raman pulses. Figure 5.6 shows the comparison with and without the feedforward.

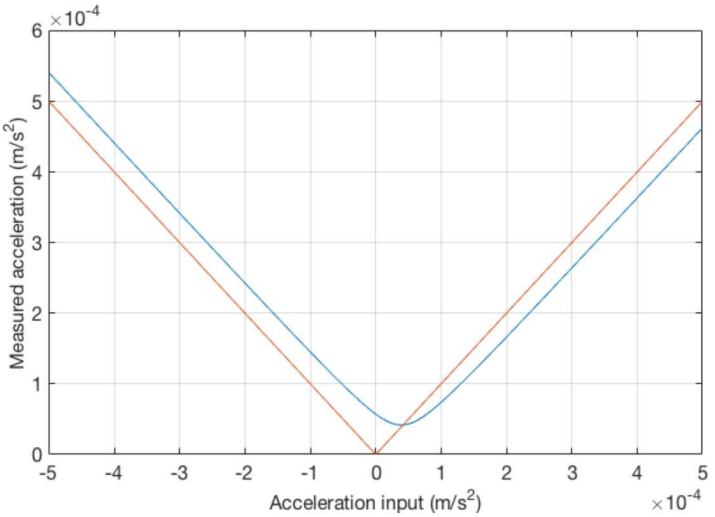

Figure 5.6: Measured acceleration values with feedforward (red) and without feedforward (blue) $\delta(t) = \delta_m(t)$ for various input acceleration values.

5.6 Noise canceling performance

As we have understood the effect of the atom movement that appears in two-folds: (1) Doppler shift for k_1 and k_2, and (2) phase drift during the Raman pulses, we are in a very good position to revisit the noise canceling feedforward scheme and see the efficacy of the feedforward in the context of moving atoms.

The noise-canceling feedforward can be designed very efficiently now combined with the atom-movement feedforward. To be clear, the feedforward scheme is now $\delta(t) = \delta_m(t) + \Delta\delta_i$ where $i = 2, 3$ and $\Delta\delta_i$ are defined in equations (4.5) and (4.6), while $\delta_m(t)$ is defined in (5.21), which must be modified considering the Doppler shift as

$$\delta_m(t) = \frac{k_1(v_g) + k_2(v_e)}{2t} a(t - t_0)^2 + \frac{1}{t}(k_1(v_g)v_{g0} + k_2(v_e)v_{e0})(t - t_0), \tag{5.23}$$

where

$$k_1(v_g) = \left(1 - \frac{v_g}{c}\right) k_1, \quad k_2(v_e) = \left(1 + \frac{v_e}{c}\right) k_2. \tag{5.24}$$

Obviously this feedforward scheme requires knowledge of a (v_{g0}, v_{e0} are calculated from a), which must rely upon the best estimate of a. For example, a simple way is to use the measured a in the previous instance of the AI accelerometer output.

In addition, from equation (4.1), we can calculate the feedforward scheme to cancel the noise by adding

$$\delta_N(t) = \frac{k_1(v_g) + k_2(v_e)}{t} \int_0^t \mathrm{d}t' \int_0^{t'} \mathrm{d}t'' a_N(t''). \tag{5.25}$$

Note that, in order to calculate the above quantity, one must estimate a_N. This is approximated in practice by adopting an external co-sensor that can approximately estimate a_N.

The total feedforwad is given as

$$\delta(t) = \delta_m(t) + \delta_N(t). \tag{5.26}$$

We set the input acceleration to be 1×10^{-3} m/s^2. The noise amplitude is 1/10 of the input amplitude, for various noise frequencies and phases. We analyze the noisy output using the concept of the normalized r.m.s. error (the r.m.s. error acceleration over various noise phase for a fixed noise frequency, divided by the input acceleration).

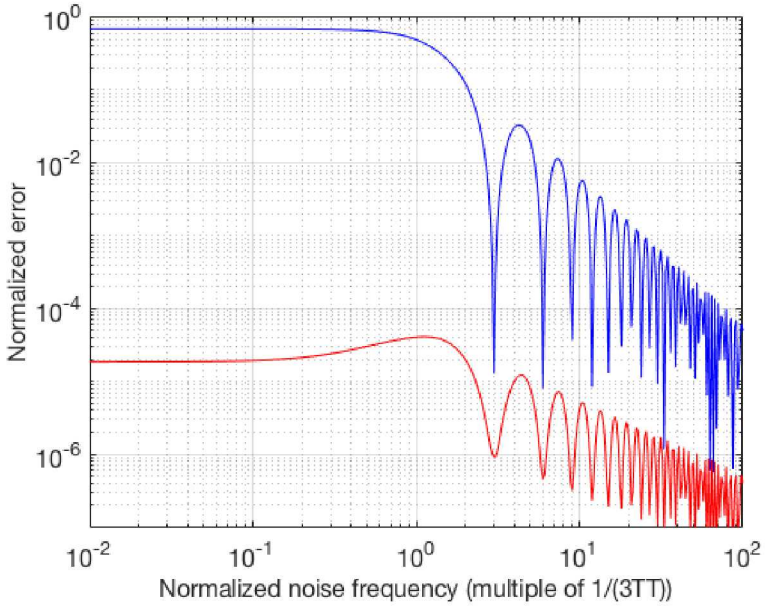

Figure 5.7: The normalized r.m.s. error over the noise phase (i.e., the r.m.s. error in m/s^2 divided by the input noise amplitude) for various noise frequencies, with (red) and without (blue) the feedforward scheme.

We then perform the noise analysis for various noise frequencies and noise phases as before. Figure 5.7 shows the result. The first figure shows the comparison between the case with and without the feedforward combo of the noise canceling and atom movement canceling schemes. We see that the this combo-feedforward scheme reduced the noise by eight orders-of-magnitude, which can be favorably compared with only five orders-of-magnitude noise suppression (c.f. figure 4.5).

We note that the noise canceling feedforward in equation (5.26) is updated every 67 ps (15 MHz). The figure exhibits several important information. First of all, the uncompensated error curve (blue) shows plateau up to the noise frequency $1/3T$. Then, it polynomially decreases as the noise frequency increases. This is understandable due to the averaging effect for fast noise frequencies. Then, the blue curve also exhibits singularly small noise output at frequency multiples of $1/T$, such as $1/T, 2/T, 3/T$, etc. The interpretation is simple: when the noise is synchronized exactly with the interval T between the two Raman pulses, the effect is reduced since the position of atoms at the moment of the Raman pulses is not deterred.

When the feedforward is applied, the output noise is five orders-of-magnitude smaller than the case without the feedforward. The root cause of the remaining small error is still under investigation.

An in-depth investigation of the remaining errors shown in the above numerical simulation revealed that, the outcome with the feedforward noise canceling is limited by the machine-precision of the Matlab simulator. Unfortunately, Matlab supports only 'double'

precision (using 64 bits)[2] that allows only $\sim 10^{-16}$ precision in the fraction (52 digits), while one digit is for the sign and the remaining 11 digits are used for the exponent. It was found that the noise canceling feedforward successfully suppressed the noise up to 10^{-16} precision, while the remaining fraction affected the output error. Hence, to the machine-precision of Matlab, this feedforward with the ideal parameter identification performance (i.e., perfectly knowing the real-time acceleration $a(t)$), this feedforward scheme efficiently suppresses the noise.

In fact, the feedforward scheme cannot perfectly cancel the effect of noise due to the following two reasons. Firstly, the system dynamics represented in equations (3.1), which are repeated here:

$$\dot{\tilde{c}}_g = i\frac{|\Omega_1|^2}{\Delta}\tilde{c}_g + i\frac{\Omega_1\Omega_2^*}{\Delta+\delta}\tilde{c}_e e^{i(\boldsymbol{k}_2\cdot\boldsymbol{x}_e - \boldsymbol{k}_1\cdot\boldsymbol{x}_g+\delta t)},$$
$$\dot{\tilde{c}}_e = i\frac{\Omega_1^*\Omega_2}{\Delta}e^{i(\boldsymbol{k}_1\cdot\boldsymbol{x}_g - \boldsymbol{k}_2\cdot\boldsymbol{x}_e-\delta t)}\tilde{c}_g + i\frac{|\Omega_2|^2}{\Delta+\delta}\tilde{c}_e.$$

clearly contain the feedforward $\delta(t)$ in the factor for $\tilde{c}_e$. Therefore, this leaves unintended error. Secondly, the π pulse duration (and the $\pi/2$ pulse duration) is a function of δ as well. Note that the π pulse duration is $T_\pi = \pi/D'$ with D' given in equation (2.18), which is repeated here:

$$D' = \sqrt{\frac{(|\Omega_1|^2+|\Omega_2|^2)^2}{\Delta^2} + \delta^2 + 2\frac{\delta}{\Delta}(|\Omega_2|^2 - |\Omega_1|^2)}.$$

Hence, changing δ indeed affects the ideal π pulse (and $\pi/2$ pulse) duration. This also leaves undesired back-action of the feedforward. To counter this back-action, one must adjust the π and $\pi/2$ pulse duration according to the varying δ values.

In fact, a way around for the machine-precision problem is to completely cancel the accumulated effect of the noise from the phase term. This can be accomplished by setting the noise acceleration a_N to be zero, only for the calculation of phase term Δ_{kx}. Figure 5.8 shows the result, which shows the comparison between the case with and without the feedforward. Clearly, the effect of the coefficient of $\tilde{c}_e$ is shown to exhibited the non-ideally suppressed noise at the order-of-magnitude of $\sim 10^{-8}$ for the low frequency, which however reduces down polynomially, following the trend of the case without the feedforward.

We also resolved the impact of D' by the varying δ values. This can be accomplished to forcefully modify the coefficient of $\tilde{c}_e$ in the dynamics from $i|\Omega_w|^2/(\Delta+\delta)$ to $i|\Omega_2|^2/\Delta$. We performed the simulation on this modified dynamical equation, and we found that, the effect on the imperfection of the duration of $\pi/2$ and π pulses by the varying δ values is not shown within the machine-precision of Matlab. The reason is that the first term of D' inside the square-root is truly dominant by a factor of $\sim 10^8$, compared to δ^2. The Taylor expansion is $\Delta' \approx A + \delta^2/2A$, where $A \sim 4.7\times 10^6$. With $\delta \sim 10^3$, the difference is only in the order of 10^{-7}, which does not appear to affect significantly.

Therefore, the dominant non-ideal back-action is from the coefficient of $\tilde{c}_e$, which dictates the remaining unsupressed noise at $\sim 10^{-8}$ relative order-of-magnitude.

[2]With the 'symbolic toolbox', it appears that one can increase the precision much higher.

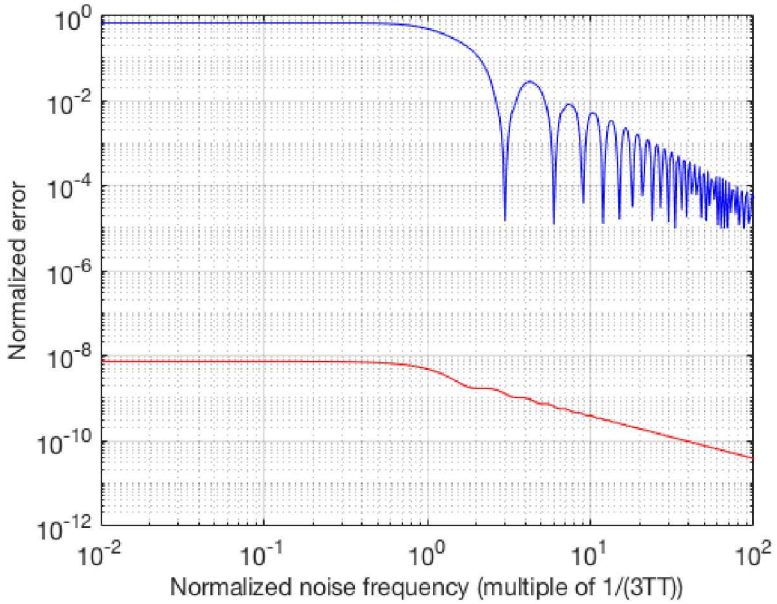

Figure 5.8: Comparison the cases without (blue) and with a perfect feedback. The red curve is the outcome of the combined effect of the factor of $\tilde{c}_e$ and the small effect on D' (see the text).

6 The multi-atom Monte-Carlo simulation

6.1 Description of thermally distributed initial velocities

We are in a position to discuss the realistic multi-atom simulation. The temperature of prepared cold atoms dictates the initial velocity distribution among many atoms. As we discussed in the previous section, the initial velocity greatly affects the measured acceleration, mainly because the atoms move during the Raman pulses and blur the phase. It will be interesting to see the effect of the temperature on the 'averaged' measured acceleration among many atoms.

Briefly, the temperature and the initial velocity is best understood through the thermal velocity determined by $v_{\rm th} = \sqrt{k_B T_e/M}$. where T_e is the temperature. Therefore, $v_{\rm th}$ is slowly dependent on the temperature.

We ran an example of Monte-Carlo simulation of the atoms having random initial velocity according to the Boltzmann velocity distribution in equation (5.18), for 1D system. As a test drive, we set the number of atoms to be 10^4. We set the temperature as 50 μK, having a thermal velocity (standard deviation of the normal distribution) of 0.07 m/s. The distribution of the initial velocity is shown in figure 6.1 (a). With 10^4 number of atoms, still the distribution is rough. Then, we ran the simulation for each of 10^4 atoms and found the distribution of the measured acceleration in figure 6.1 (b). The distribution is not symmetrical centered at the average, due to the asymmetrical influence of the initial velocity as shown in figure 5.5 (a). The average and the standard deviation of the measured acceleration are 1.05×10^{-3} m/s^2 and 3.86×10^{-4} m/s^2, respectively.

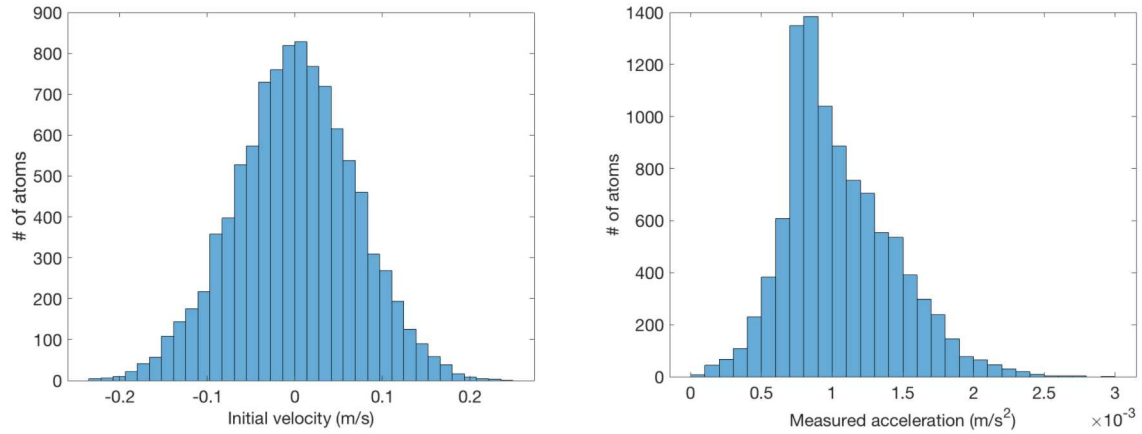

(a) Initial velocity (b) Measured acceleration

Figure 6.1: The initial velocity distribution for $T_e = 50\ \mu$K (a), and the measured acceleration distribution (b). Monte-Carlo simulated with 10^4 atoms.

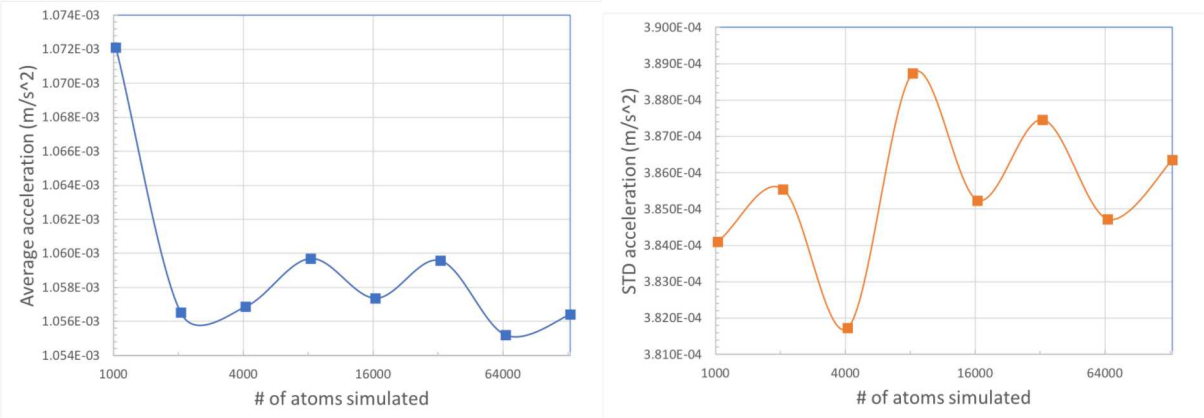

(a) Measured average (b) Measured standard deviation

Figure 6.2: Statistical quantities of the Monte-Carlo simulation as a function of the number of simulated atoms.

6.2 Statistical validity of Monte-Carlo simulation

We also performed the basic checking of the statistical validity of the Monte-Carlo simulation. The usual way is to see if the statistical quantities such as the average and the standard deviation over the atoms converge as we increase the number of atoms. The result is shown in figure 6.2. Up to 1.3×10^6 number of atoms simulated, the average and the standard deviation of the measured acceleration reasonably converged. The simulation time for 1.3×10^6 number of atoms was 13 minutes on a 4-core modern computing machine with 8 GB memory. With 1.3×10^6 number of atoms, the average is correct within 0.1% error and the standard deviation is within 0.3% error.

6.3 Effect of initial temperature of atoms

We then performed the temperature sweep to understand the effect of the temperature on the measured acceleration. Figure 6.3 shows the result. When the temperature is

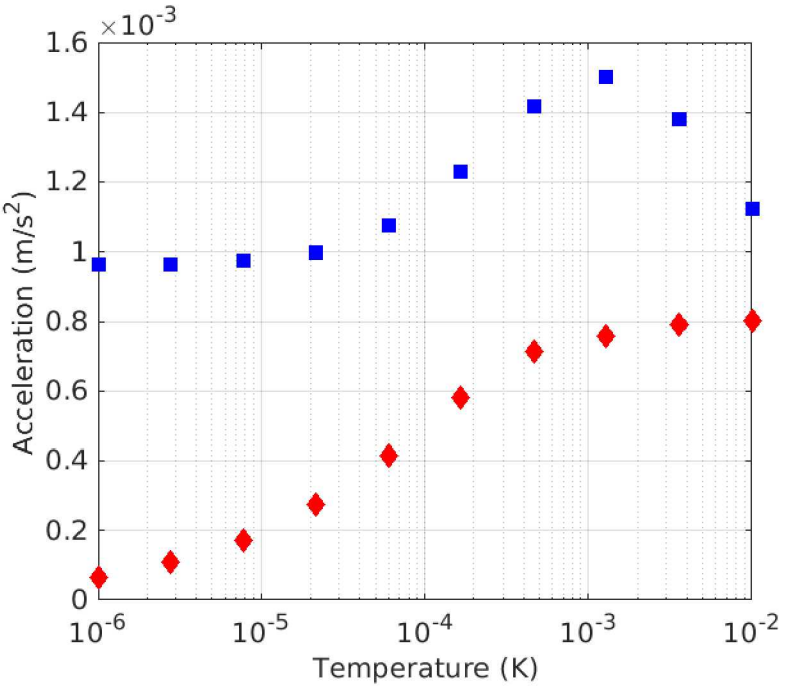

Figure 6.3: Monte-Carlo simulation for various temperature values. Blue squares: averaged measured acceleration over $2^{14}(\sim 1.6 \times 10^4)$ atoms, red diamonds: standard deviation of measured acceleration over the same number of atoms. The induced acceleration was 1.0×10^{-3} m/s^2. Each simulation resulting a pair of dots took 2 minutes using a 4-core modern computing machine.

1 μK, the measured averaged temperature over $2^{14}(\sim 1.6 \times 10^4)$ atoms is 9.62×10^{-4} m/s^2, which is consistent with the single atom with zero initial velocity (see the figure 5.1). The standard deviation of the individual acceleration measurement on each atom is 6.42×10^{-5} m/s^2, which is quite narrow. As the temperature increases, both the average and the standard deviation are affected. Particularly when the temperature is over 10 μK, the average starts increasing and the standard deviation also starts rapidly increasing. When the temperature is near 100 μK, the standard deviation is over the half value of the averaged temperature. As one might guess from the independent study of the effect of the initial velocity (see figure 5.5 (a)), when the initial velocity distribution is wide, the measured acceleration is no longer linear with respect to the initial velocity. Then, the collective measurement of the thermally distributed atom velocities will result in deviation from the ideal value. Hence, the initial temperature of atoms must be impeccably low (preferably below μK).

One thing to note here is that, in reality, the quantity that is averaged over multiple atoms is not the measured acceleration, but the populations $|c_g|^2$ and $|c_e|^2$, which enters collectively to the equation (2.35). However, it is expected that the qualitative behavior will be similar whether one takes the average after the equation (2.35) or before it. The actual values will be different, though, since the formula in equation (2.35) is certainly nonlinear.

Acknowledgement

Sandia National Laboratories is a multimission laboratory managed and operated by National Technology & Engineering Solutions of Sandia, LLC, a wholly owned subsidiary of Honeywell International Inc., for the U.S. Department of Energy's National Nuclear Security Administration under contract DE-NA0003525.

References

[1] Akash Rakholia. High data-rate atom interferometry for measuring dynamic inertial conditions, 2015.